

POLITECNICO DI TORINO

Master's Degree in Nanotechnology for ICT



**Integration of Engineered Nano-Graphitic
Carbon Sensors and Detection Circuitry
for Enhanced Dopamine Sensing**

Supervisors:

Prof. Carlo RICCIARDI

Prof. Davood SHAHRJERDI

Dr. Edoardo CUNIBERTO

Candidate

Davide FRANCO

July 2023

Abstract

In recent years, the rapid advancement of point-of-care (POC) and wearable/implantable devices has brought about significant transformations in healthcare delivery. These innovative technologies provide real-time monitoring, diagnosis, and treatment capabilities, thereby enhancing patient care, improving disease management, and reducing healthcare costs. Within this context, carbon sensors have emerged as promising tools due to their high electron mobility, excellent thermal conductivity, and large surface area. Among them, nano-graphitic (NG) carbon sensors have demonstrated success in constructing densely packed arrays of miniaturized electrochemical sensors at the micron-scale level, exhibiting exceptional performance in detecting low concentrations of bio-analytes.

The aim of this work is divided in two. The first is to establish protocols for the fabrication of metal-induced NG sensors and execute proof-of-concept experiments to investigate the diverse effects of various parameters related to the production process on the structural and morphological characteristics of these sensors, which were analyzed through Raman and optical analysis during this phase. The second is to develop and implement the necessary detection circuitry for interfacing with the biosensors. The circuitry is responsible for signal amplification and digitization. Two potential analog front-end (AFE) circuits were considered, both of which were implemented on a printed circuit board (PCB) and subsequently compared and tested. Additionally, a second version of the AFE was designed to enable multichannel reading. Furthermore, concepts for the digitization component of the circuit (analog-to-digital converter, ADC) and its mechanisms will be explored to gain a deeper understanding of key project parameters.

Finally some fast scan cyclic voltammetry (FSCV) measurements have been made in a microfluidic chamber in order to detect note concentrations of dopamine in a phosphate buffered saline solution (PBS) to confirm the capability of the produced biosensors. Scanning electron microscopy (SEM) and atomic force microscopy (AFM) images have been taken to check the morphology and roughness.

Table of Contents

List of Tables	VI
List of Figures	VII
1 Introduction	1
1.1 Project Aim	2
1.2 Structure of the Work	2
2 NG Sensors	5
2.1 Theoretical introduction	5
2.1.1 Electrochemical sensing of dopamine	5
2.1.2 NG Sensor Concepts	6
2.1.3 Cyclic Voltammetry and Fast Scan Cyclic Voltammetry	9
2.1.4 Raman Spectra of Graphitized Structures	11
2.2 NG Island Preparation: Methods and Setup	12
2.2.1 Chemicals	12
2.2.2 Sample Preparation	13
2.2.3 Setup description	13
2.2.4 Carbonization and Graphitization	13
2.3 Tuned parameters and Proof of Concept Experiments	15
2.4 FSCV Setup and Measurements	19
2.4.1 Setup Description	19
2.4.2 Conditioning	20
2.4.3 Results	21
2.5 AFM and SEM images	22
3 Detection Circuitry	26
3.1 Theoretical introduction	26
3.1.1 Noise and Signal to Noise and Distortion Ratio	26
3.1.2 Power Spectral Density and Integrated Voltage Noise	27
3.1.3 PCB Design	29

3.2	Project Parameters and Concepts to Select an ADC	31
3.3	Description of the First Board	33
3.3.1	Trans Impedance Amplifier stage	35
3.3.2	Programmable Gain Amplifier stage	36
3.3.3	Instrumentation Amplifier stage	37
3.3.4	Filtering Stages	38
3.4	Tests on the First Board	38
3.4.1	Signal Generator Noise Check	39
3.4.2	Board Noise	39
3.5	Description of the Second Board	41
3.6	Test on the Second Board	41
4	Conclusions	44
	Bibliography	46

List of Tables

2.1	System specification for measuring phasic (RPS) and tonic (SPS) dopamine using NG micro-sensors. Reprinted from [10].	8
2.2	Reported the parameters used for the graphitization phase of the fabricated sensor. They represent the baseline for the investigation of the parameters presented in this section.	16
3.1	Description of the fundamental blocks constituting the 4 channels of the first board. All the filters reported in the table are active filters. Note T.P. stands for testing points.	34
3.2	Integrated noise over the interested bandwidth (0 to 5 kHz) in RMS values referred to the output voltage and reported to the input current for board 1.	41
3.3	Integrated noise over the interested bandwidth (0 to 5 kHz) in RMS values referred to the output voltage and reported to the input current for board 2.	42

List of Figures

2.1	Skeletal formula of dopamine (4-(2-Aminoethyl)benzene-1,2-diol). . .	6
2.2	The main phases of the NG sensor fabrications are reported comprising the SU-8 deposition (a), EBL island patterning and carbonization (b), metal deposition for the graphitization (c), and the final NG sheets obtained at the end of the graphitization step. Reprinted from [9].	7
2.3	Functionalization steps to add insulated metal contacts to the NG carbon islands. (a) displays a schematic lateral projection of the sensor while (b) shows an optical image of a sensor sample seen from the top. (c) Cross-sectional schematic of the experimental setup for FSCV measurements of dopamine. Reprinted from [10].	8
2.4	Figure 2.4a displays a set of voltammograms illustrating different electrochemical responses. The x-axis represents the applied potential between the reference electrode and the working electrode in a 3-electrode electrochemical cell. The y-axis represents the corresponding current measured on the counter electrode. Figure 2.4b presents the US and IUPAC conventions for CV measurements. Reprinted from [17].	9
2.5	Figure 2.5a represents a schematic illustration of a triangular potential waveform. The potential is varied linearly in time between a lower potential limit (LPL) and an upper potential limit (UPL). Figure 2.5b displays the I-V characteristic of the background current plus redox while in Figure 2.5c the background current has been removed leaving the dopamine signal only. Reprinted from [10]. . .	10
2.6	Comparison between the typical Raman spectra of carbon based materials (right) respect to the graphitized ones (left). For graphitized materials an additional peak is present, namely the 2D peak. Reprinted from [19].	11
2.7	Scheme of the setup for the Carbonization and Graphitization annealing phases.	14

2.8	To the left is displayed the schematic of the vertical stack structure loaded in the furnace for the graphitization phase. To the right an optical image of the islands after being graphitized.	15
2.9	Effect of the different concentration of the iron chloride solution on the Raman spectrum.	17
2.10	Effect of graphitization time on the Raman spectrum.	17
2.11	Effect of the Argon-Hydrogen flow on the Raman spectrum.	18
2.12	Effect of the spacers thickness on the Raman spectrum.	18
2.13	Effect of the internal preassure of the furnace on the Raman spectrum.	19
2.14	To the left is reported a photograph of the in-vitro measurement setup, to the right a scheme of the y-shaped microfluidic chamber. (b) is reprinted from [10].	20
2.15	Confrontation of the Raman spectrum before and after the conditioning phase.	21
2.16	(a) Voltammograms obtained during the detection of dopamine and during the detection of PBS only. (b) Resulting CV of the dopamine detection after the removal of the background signal.	22
2.17	Voltage dependence of current at the reduction (a) and oxidation peak(b). The dashed line serves as a guide for the eye, representing the linear interpolation of the points.	23
2.18	AFM images of the two sister islands and related measured profile. On the left the island that did not underwent conditioning is thicker respect to the one that did (right).	23
2.19	SEM image of the islands after the preliminar conditioning phase for FSCV measurments. To the left is reported the sister island which has not undergone conditioning while on the right the tested island.	24
3.1	Representation of the power spectrum of a reference signal. In blue the power of the frequency carrying the signal is reported, while in red the noise plus distortion contribution are represented. Reprinted from [22].	27
3.2	Representation of a sinusoidal signal in time domain on the left and its resultant Fast Fourier Transform (FFT) on the right. Because negative frequencies are not physically measured, DFT is usually redefined only between 0 and half the Nyquist frequency.	28
3.3	Representation of the stackup of a general PCB. The stackup consists of alternating conductor and dielectric planes; usually the external conducting planes are used for the signal part while the internal ones are reserved for ground. Particular cases and more complicated stackup structures may be different.	30

3.4	Board design after completing the routing step. It is possible to see how the footprints of every component presents metal leads that will be connected through routes. Reprinted from [24].	31
3.5	Last phase of the PCB production: component placement and soldering.	32
3.7	Third channel of the Board composed by a TIA stage plus an IN-AMP stage. A test point has been added after the TIA, IN-AMP and HPF to verify the signal during the testing phase. The circuit final part is a second order HPF followed by a second order LPF. . .	34
3.6	First channel of the Board composed by a TIA stage plus a PGA stage. A test point has been added after the TIA to verify the signal during the testing phase. The circuit final part is a first order active LPF.	35
3.8	Schematics representing the R-TIA module. Reprinted from [26]. . .	36
3.9	Resistor array PGA. Reprinted from [28].	37
3.10	Photos of the noise test setup.	39
3.11	Variation of the Signal to Noise and Distortion Ratio (SNDR) of the measured signal in function of its amplitude. The crossing point on the x axis represents the maximum ratio between signal and noise, without taking into account the distortion.	40
3.12	In blue is reported the PSD of the DAQ, while in red is reported the PSD of the total system (channel1 plus DAQ).	40
3.13	Schematics of the first two channels of the second board. The connections for the dummy sensor are also reported. The board consists of 8 channels and, apart for the first having additional testing points, all the additional channels present the same structure as the second one.	42

Acronyms

ADC Analog to Digital Converter.

AFE Analog Front End.

AFM Atomic Force Microscopy.

CV Cyclic Voltammetry.

DFT Discrete Fourier Transform.

EBL Electron Beam Lithography.

ENOB Effective Number of Bits.

FDA Fully Differential Amplifier.

FFT Fast Fourier Transform.

FSCV Fast Scan Cyclic Voltammetry.

HPF High Pass Filter.

IN-AMP Instrumentation Amplifier.

LPF Low Pass Filter.

LPL Lower Potential Limit.

NG Nano Graphitic.

Op-Amp Operational Amplifier.

PBS Phospate-Buffered Saline.

PCB Printed Circuit Board.

PGA Programmable Gain Amplifier.

PSD Power Spectral Density.

RPS Rapid Potential Sweep.

RTI Refereferred-to-input.

SB Signal to Background.

SEM Scanning electron Microscopy.

SNDR Signal to Noise and Distortion Ratio.

SNR Signal to Noise Ratio.

SOI Silicon on insulator.

THD Total Harmonic Distortion.

TIA Trans Impedance Amplifier.

UPL Upper Potential Limit.

Chapter 1

Introduction

Micro-nanomaterials have emerged as a pivotal field in scientific research and technological advancements, providing unprecedented opportunities for developing innovative materials and devices with unique properties. Among the wide range of micro-nanomaterials, graphene and graphite have gained significant attention due to their exceptional structural, electrical, and thermal characteristics. Graphene, a single layer of carbon atoms arranged in a hexagonal lattice, exhibits extraordinary mechanical strength, high electrical conductivity, and remarkable thermal properties. On the other hand, graphite, composed of stacked graphene layers, possesses excellent lubricity and electrical conductivity.

The exceptional properties of graphene and graphite have propelled their integration into various technologies and applications. In the realm of electronics, graphene's high electron mobility and conductivity make it an ideal material for transistors [1], flexible wearable[2], and high-speed electronic devices [3]. Graphite finds extensive use as an electrode material in lithium-ion batteries [4], as a lubricant in industrial applications [5], and as a moderator in nuclear reactors [6]. Electrochemical sensors, a critical branch of sensing technology, have experienced remarkable advancements with the advent of carbon-based sensors. Carbon sensors, including nanotube and Nano Graphitic (NG) carbon sensors, have revolutionized the field of electrochemical sensing. These sensors leverage the high electron mobility and large surface area of carbon materials to achieve exceptional sensitivity in detecting various analytes. Carbon sensors find applications in diverse fields, such as environmental monitoring [7], biomedical diagnostics [8], food safety, and industrial process control. The unique properties of carbon sensors enable them to detect and quantify analytes with high precision and accuracy. For instance, carbon sensors have been utilized for dopamine sensing [9], enabling the monitoring and diagnosis of neurological disorders like Parkinson's disease. The continuous advancements in micro-nanomaterials, graphene, graphite, and carbon sensor technologies open up new possibilities for developing advanced sensing platforms, wearable

devices, energy storage systems, and more. These innovations hold the potential to revolutionize industries and improve the quality of life through enhanced sensing capabilities and advanced materials engineering.

1.1 Project Aim

The aim of this project is to develop NG sensors for real-time enhanced dopamine sensing applications based on the works of [10]. To achieve this, a robust detection circuitry is essential, capable of amplifying and digitizing the sensor signal. Microfabricated sensors play a crucial role in supporting Cyclic Voltammetry (CV) experiments. Their miniature size and precise fabrication allow for efficient and controlled measurements of the redox current associated with dopamine detection. By utilizing microfabricated sensors, researchers can achieve high spatial resolution and accurate monitoring of dopamine levels, enabling advancements in neurochemical research and disease diagnosis. The fabrication method of the NG sensors is based on the work of [10], [9]. The main novelty, is the utilization of iron as a metal catalyst in the graphitization phase which will benefit the sensor composition for the in-vivo experiments, because of the bio-compatibility of iron against the toxicity of nickel. The ultimate goal of the technology is to become a brain sensor for real time dopamine detection, so the bio-compatibility becomes crucial for the sensors. The iron catalyst is applied to the sensor with simple techniques, not requiring the utilization of deposition steps performed in clean room (as done for the Ni deposition), saving time and reducing the costs. The focus is in the growth of the NG sensor while developing protocols and performing proof-of-concepts experiments. Another objective is the realization of an interface circuit used as a multichannel, giving the possibility of real time detection of multiple sensors. The main intent is too reduce noise in the system in order to achieve a limit of detection of dopamine as low as possible, to detect nano molar concentrations.

1.2 Structure of the Work

This work will be structured in two main chapters, one based on the creations and measurements taken on the NG sensors while the other will focus on the development of the Analog Front End (AFE) for the circuit interfacing the sensors. In the sensors chapter a theoretical introduction about electrochemical sensing of dopamine, the operation and basic concepts about the NG sensors, CV concepts with particular focus on Fast Scan Cyclic Voltammetry (FSCV) and an explanation of the Raman spectra of graphitized structures will be provided. Then the detailed preparation of NG sensors are reported, while the effects many parameters during the fabrication phase are investigated. Finally the FSCV measurements of the

dopamine detection are reported, followed by Atomic Force Microscopy (AFM) and Scanning electron Microscopy (SEM) images to check the final sensor structure and morphology. In the circuit chapter a theoretical introduction about noise, in particular Signal to Noise and Distortion Ratio (SNDR), Power Spectral Density (PSD) and Voltage noise, is presented. Then the project parameters of the circuit will be given along with a few concepts to select an Analog to Digital Converter (ADC) right for our application. Two Printed Circuit Board (PCB) have been designed for the AFE circuit, one the evolution of the other. The boards structure is presented while their noise is investigated. A final conclusion chapter closes the work, retracing the results obtained and analysing future steps.

Chapter 2

NG Sensors

2.1 Theoretical introduction

The introduction will cover the basic concepts around which the NG sensor will operate in the detection of dopamine. Specifically, a brief general introduction about dopamine and some hints about its electrochemistry will be reported for the purpose of providing a framework for the measurements performed at the end of chapter. Then some concepts about the NG sensors and their fabrication will be presented, with particular emphasis on a few practical arrangements for tests or circuit integration purposes. Finally a presentation of the CV method, in particular FSCV method, will follow.

2.1.1 Electrochemical sensing of dopamine

Dopamine (Figure 2.1) is a crucial neurotransmitter in the human central nervous system and plays a vital role in the reward circuits of the brain [11], influencing motivation, pleasure, and reinforcement. Beyond its impact on the central nervous system, dopamine also exerts effects on various other physiological systems, including the renal, cardiovascular, and hormonal systems [12]. Low levels of dopamine have been associated with neurological diseases such as Parkinson's disease, schizophrenia, Alzheimer's disease, and depression. Furthermore, inadequate dopamine signaling can contribute to elevated stress levels, highlighting the wide-ranging importance of dopamine in both neurological and physiological processes.

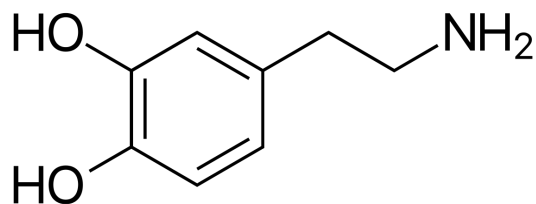


Figure 2.1: Skeletal formula of dopamine (4-(2-Aminoethyl)benzene-1,2-diol).

Therefore a fast, accurate, simple and low cost and easily applicable method is needed to measure its concentration in pharmaceutical applications and biological fluids. Several methods can be used to detect dopamine, such as molecular recognition ones based on enzymes, antibodies, and aptamers as well as new advances based on nanomaterials and molecularly imprinted polymers [12]. A significant proportion of these sensors utilize electrochemical detection to meet the demand for rapid, in situ, and in vivo detection, while achieving high spatial and temporal resolution.

In brain, changes of dopamine concentration occur at two different temporal scales: tonic and phasic [13]. The tonic mode represents the extracellular level of the baseline dopamine that changes slowly over minutes to hours. In contrast, the extracellular dopamine level in the phasic mode changes rapidly, on the order of seconds [10].

2.1.2 NG Sensor Concepts

NG sensors have emerged as a promising class of sensors with unique properties, offering vast potential in various sensing applications. The sensors analyzed in this study originate from a planar structure made of amorphous carbon, which can be graphitized through metal-induced graphitization techniques [14]. These techniques utilize metal catalysts to promote the transformation of amorphous carbon into graphitic carbon while avoiding the restrictions on the production temperature due to the thermal stability restriction of silicon substrates (1100°C), which would result in fully disordered carbon structures with slow electron transfer kinetics. Crucially, the density of point defects in the resulting nano-graphitic structure plays a pivotal role in sensing applications. Increasing the average density of point defects enhances the sensitivity per unit area of the sensors, making them highly suitable for detecting and analyzing redox reactions [9].

The sensors fabrication starts depositing a SU-8 layer on top of thermally grown SiO_2 substrate, which will then be patterned through e-beam lithography, compensating the dangers of graphene transfer techniques. Two fundamental steps will follow namely the carbonization and graphitization phases. Carbonization is

basically an annealing step that converts polymeric films of SU-8 into amorphous sp^2 hybridized carbon while graphitization involve the deposition of a metal source and an higher temperature annealing step that converts amorphous carbon into NG sheets [15][16]. The main steps are represented in Figure 2.2. Further details about the carbonization and the graphitization are described in the methods and setup section.

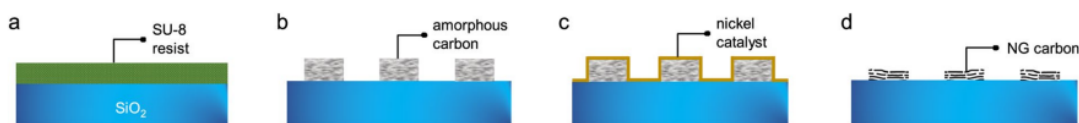


Figure 2.2: The main phases of the NG sensor fabrications are reported comprising the SU-8 deposition (a), EBL island patterning and carbonization (b), metal deposition for the graphitization (c), and the final NG sheets obtained at the end of the graphitization step. Reprinted from [9].

At this stage the NG carbon islands are ready to be made into functional devices. To accomplish this, standard nano-fabrication techniques are utilized to fabricate Cr/Au metal contacts and insulating SU-8 protection layers. The process involved the creation of metal contacts using Cr/Au through established fabrication methods, followed by the formation of protective SU-8 layers to insulate the metal leads (to get signal only from the sensor). This approach ensured reliable electrical connections and prevented contact between the metal and the solution during experimental procedures. A schematic and optical image of the functionalization stage are shown in Figure 2.3. Note from Figure 2.3 (b) that four islands are grouped together; from left to right the first two islands possess an area of $360 \mu m^2$ while the other two possess an area of $580 \mu m^2$. This is done to later investigate the effect of the area on the FSCV experiments. The 2 islands forming a group with the same area are called "sister" islands and usually just one of the two is connected to leads. During the FSCV the island connected to leads undergoes an additional phase called conditioning (consisting of an electrochemical etching due to the high voltages) that changes its structure and morphology. The sister island is used as a comparison after this phase.

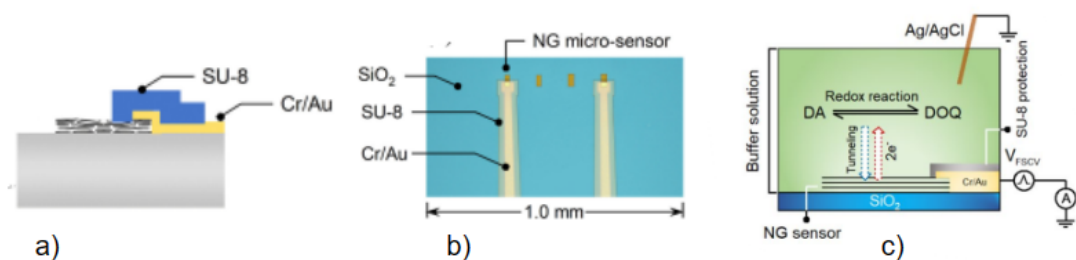


Figure 2.3: Functionalization steps to add insulated metal contacts to the NG carbon islands. (a) displays a schematic lateral projection of the sensor while (b) shows an optical image of a sensor sample seen from the top. (c) Cross-sectional schematic of the experimental setup for FSCV measurements of dopamine. Reprinted from [10].

One of the islands on the sample is usually completely covered with SU-8. This island is called "dummy" island (also called reference or noise island) and serves for measuring and monitoring environmental noise. By comparing the output of the primary sensor with the output of the dummy sensor, it is possible to separate the desired signal from the noise, enhancing the accuracy and reliability of the measurement system. A part from the NG electrode, an Ag/AgCl reference electrode is placed in the buffered solution for the FSCV experiments (see Figure 2.3 (c)).

Parameter	SPS	RPS
Minimum [DA] (nM)	100	10
Temporal Resolution (s)	10	0.1
Sensor Capacitance ($\mu F/cm^2$)	110-125*	90-100
SB Ratio ($nA \cdot \mu M^{-1} \cdot nA^{-1}$)	>0.5	>0.25
Potential Sweep Rate (V/s)	0.1	200
LPL, UPL (V)	-0.1, 0.4	-0.2, 0.6
$t_d(ms)$	0	92
$I_{cap}(nA)$	$< 80 \times 10^{-3}$	< 125
$I_{quinone}(nA)$	$< 80 \times 10^{-3}$	< 125
$I_{noise, mean}(pA_{RMS})$	< 0.4	< 32

Table 2.1: System specification for measuring phasic (RPS) and tonic (SPS) dopamine using NG micro-sensors. Reprinted from [10].

In Table 2.1 the system specification for measuring phasic dopamine under Rapid Potential Sweep (RPS) conditions are reported. From this table is possible to estimate the total capacitance of the islands, which will be useful to evaluate the

parasitic capacitance seen from the interfacing circuit and the background current resulting from the FSCV tests.

2.1.3 Cyclic Voltammetry and Fast Scan Cyclic Voltammetry

CV is a powerful electrochemical technique that allows for the investigation of redox processes and the determination of various electrochemical properties of molecules and materials. By applying a varying potential to an electrochemical cell and measuring the resulting current, CV provides valuable insights into the oxidation-reduction behavior, kinetics, and thermodynamics of species under study. Its simplicity, versatility, and ability to provide quantitative data make CV a widely used method in fields such as analytical chemistry, materials science, and electrocatalysis. In Figure 2.4a are shown the voltammograms of various analytes, everyone with its proper shape and dimensions, acting as the fingertip for every molecular species; in Figure 2.4b two conventions for the CV are shown for reference. In this work the IUPAC convention will be used.

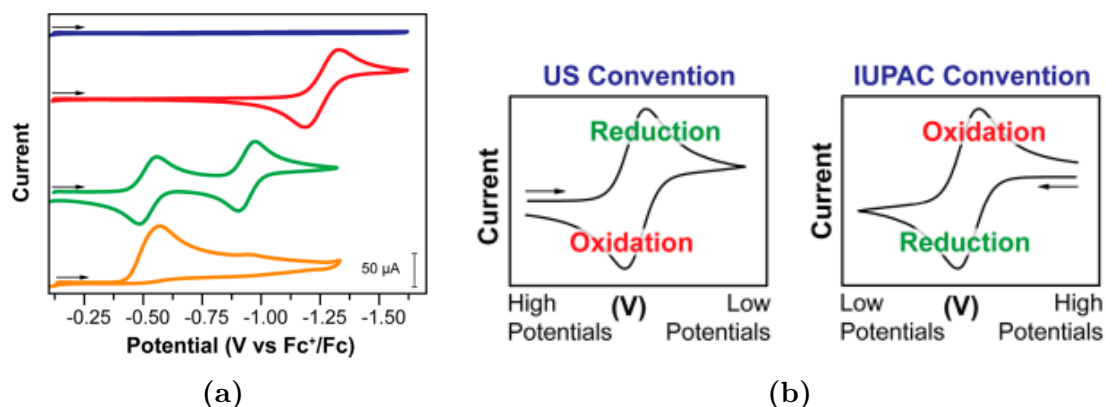


Figure 2.4: Figure 2.4a displays a set of voltammograms illustrating different electrochemical responses. The x-axis represents the applied potential between the reference electrode and the working electrode in a 3-electrode electrochemical cell. The y-axis represents the corresponding current measured on the counter electrode. Figure 2.4b presents the US and IUPAC conventions for CV measurements. Reprinted from [17].

CV consists in applying a linear variation of the potential between a Lower Potential Limit (LPL) and a Upper Potential Limit (UPL), as shown in Figure 2.5a, to the sensor and measuring the time-varying current. The above mentioned linear variation is a key parameter called scan rate (ν). As indicated in the introduction, the objective of the sensor is to detect dopamine in phasic mode therefore small

temporal resolution is needed. For this reason, FSCV will be employed. In FSCV the potential is ramped up from a holding potential to a switching potential and back, usually at a $400V s^{-1}$ scan rate and a frequency of $10Hz$ making it suitable for the fast change in neurotransmission [18]. Focusing on Figure 2.5b, I_{cap} is determined by the product of the sensor capacitance (C_{sr}) and ν . However, it is important to note that in practical scenarios, C_{sr} may not remain constant and can vary depending on the frequency of stimulation, in addition in FSCV the reaction redox is absorption-limited. To increase the absorption, the potential waveform generally includes a delay time (t_d), which is noticeably longer than t_{cv} , detrimental to the temporal resolution ($t_d + t_{cv}$) [10]. The above fact is shown in Figure 2.5a.

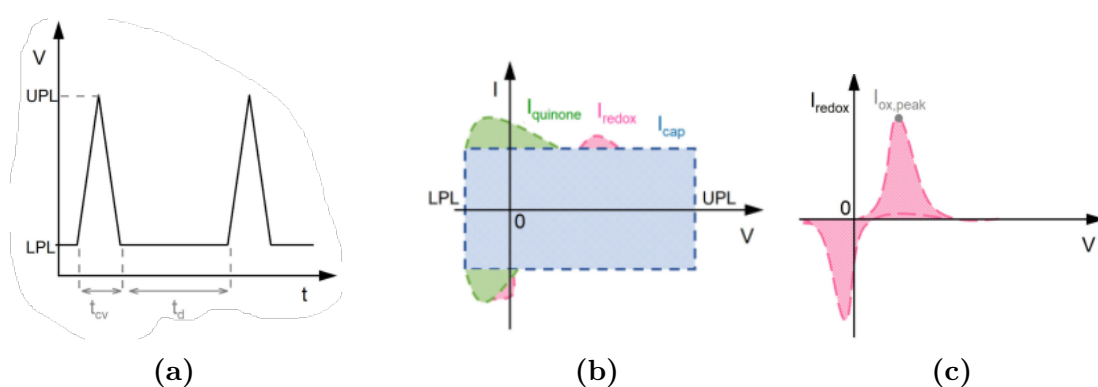


Figure 2.5: Figure 2.5a represents a schematic illustration of a triangular potential waveform. The potential is varied linearly in time between a lower potential limit (LPL) and an upper potential limit (UPL). Figure 2.5b displays the I-V characteristic of the background current plus redox while in Figure 2.5c the background current has been removed leaving the dopamine signal only. Reprinted from [10].

One of the most relevant shortcomings of this method is the presence of the background current, shown in Figure 2.5b as the sum of $I_{quinone}$ (from the oxidized state of dopamine) and I_{cap} . A common method to solve this problem is to perform a baseline correction, consisting in capture and recording the complete profile of the background signal with utmost precision. This comprehensive background signal can then be utilized for rigorous data analysis, enabling the extraction of the desired analytical information while effectively compensating for any interfering factors or noise present in the measurement system. It becomes useful to introduce the Signal to Background (SB) ratio, a critical parameter used to quantify the strength or amplitude of the desired signal relative to the unwanted noise, providing a measure of the signal's clarity and distinguishability. The SB ratio can be defined as: $SB \text{ ratio} = I_{ox,peak}/I_{cap}$.

2.1.4 Raman Spectra of Graphitized Structures

Raman spectroscopy is a versatile and powerful analytical technique widely used in various scientific fields. By illuminating a sample with light and analyzing the scattered photons, Raman spectroscopy provides valuable insights into the molecular structure, composition, and vibrational characteristics of materials. It allows for non-destructive analysis of samples in different states, including solids, liquids, and gases. The technique's ability to detect energy shifts and intensities of scattered photons enables detailed information about chemical bonds, crystal structures, and molecular interactions to be obtained. As a result, Raman spectroscopy has become an essential tool in materials science, pharmaceutical research, forensics, and environmental monitoring, offering valuable contributions to scientific understanding and technological advancements.

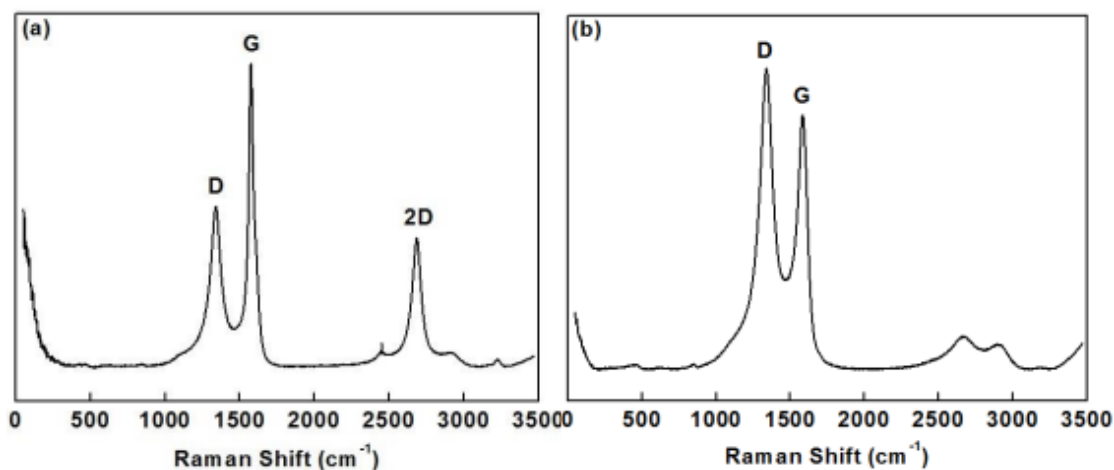


Figure 2.6: Comparison between the typical Raman spectra of carbon based materials (right) respect to the graphitized ones (left). For graphitized materials an additional peak is present, namely the 2D peak. Reprinted from [19].

A typical Raman spectra of a graphitized structure is reported in Figure 2.6(a) while a similar structure for a non-graphitized carbon based sample is shown in Figure 2.6(b). The G peak, also called graphitic peak, represents the planar configuration sp^2 bonded carbon that constitutes graphene and is also used to aid in determination of graphitic carbon. The D-band is referred to as the disorder band or defect band, it arises from the ring breathing mode of sp^2 carbon rings. However, for the D-band to be active in Raman spectroscopy, the carbon ring must be in proximity to a graphene edge or a defect within the material [20]. The intensity ratios between the D-band and G-band in Raman spectra are commonly employed as indicators for estimating the degree of graphitization in carbon-based

materials. It is well-established that a lower ratio of I_D/I_G corresponds to a higher quality and more graphitic structure [19]. Thus, a smaller I_D/I_G ratio indicates a higher proportion of graphitic carbon and a better overall graphitic structure in the material under investigation. This ratio serves as a useful parameter in assessing and comparing the graphitic quality of various carbon-based materials.

Finally the 2D-band is the second order of the D-band, it is the result of a two phonon lattice vibrational process, but unlike the D-band, it does not need to be activated by proximity to a defect. The high intensity of the 2D peak in the Raman spectrum indicates that the NG material is in stage (i) of the graphene amorphization trajectory. In this stage, the density of electronic states induced by defects is primarily non-overlapping. The prominent 2D peak intensity suggests that the NG material possesses a well-defined graphitic structure with a low density of defects and a limited degree of amorphization [9].

2.2 NG Island Preparation: Methods and Setup

2.2.1 Chemicals

All the following chemicals come from Sigma-Aldrich. Note that the last four have been employed in the Phosphate-Buffered Saline (PBS) preparation reported in the following section.

- Isopropyl alcohol (IPA) C_3H_8O
- Acetone $(CH_3)_2CO$
- Sodium molybdate Na_2MoO_4
- Iron (III) chloride $FeCl_2$
- Sulfuric Acid H_2SO_4
- Hydrogen peroxide H_2O_2
- Sodium chloride $NaCl$
- Sodium phosphate dibasic Na_2HPO_4
- Potassium phosphate monobasic KH_2PO_4
- Potassium chloride KCl

2.2.2 Sample Preparation

The sample preparation follows the method presented in [9]; the description of the sample preparation will follow from the application of the SU-8 resist and its patterning through Electron Beam Lithography (EBL) as presented in Figure 2.2 (a)-(b). At this point the sample consist of a Silicon on insulator (SOI) wafer with many rectangular-shaped SU-8 island deposited on top. Next, a cleaning phase to remove the organic/inorganic residuals is performed by immersing the sample in a becker containing acetone and then placing it inside the Mini Ultrasonic Cleaner (sonicator) by Sper Scientific Instruments for three minutes. After that the sample is washed in IPA and dried with a nitrogen gun.

2.2.3 Setup description

The core of our experimental setup consists of a Lindberg/Blue M Moldatherm Box Furnace by Thermo Scientific connected to a $Ar - H_2(80\% - 20\%)$ gas tank from Airgas at the inlet side, and to a 6826 vacuum pump from Thermo Scientific to the outlet side. Between the furnace and the gas tank, a pressure regulator and a SmartTrak 100 flowmeter from Sierra to handle the flow in the quartz tube of the furnace. At the outlet, the path of the inert gas can be switched from the pump to the atmospheric pressure which will be useful for the graphitization phase. A visual reference of the setup is presented in Figure 2.7. When the pump is switched on, the internal pressure is 2 mTorr or 260 Pa. The furnace is usually kept at 150°C to avoid contamination from water vapor.

2.2.4 Carbonization and Graphitization

The carbonization phase involves the process of transforming a carbonaceous material (SU-8), into carbon through pyrolysis. As the temperature increases, the organic components undergo thermal decomposition, leading to the release of gases and the formation of a carbon-rich structure, usually amorphous carbon. Before starting the actual carbonization, an overpressure step has to be done. This last consists of increasing the preassure inside of the system before loading the sample in order no to contaminate the tube when the sample is being loaded. With the same aim and same methodology, a purge step is done after the loading. The actual carbonization consists of bringing the system to vacuum, while a flow of 100 sccm (standard cubic centimeters per minute) crosses the furnace. The temperature is brought to 450°C with a ramp-up of 20°C/min and kept for 1 hour (75 minutes considering the ramp-up). At the conclusion of the carbonization, the system is allowed to cool naturally and the sample is unloaded after an overpressure step and checked under an optical microscope.

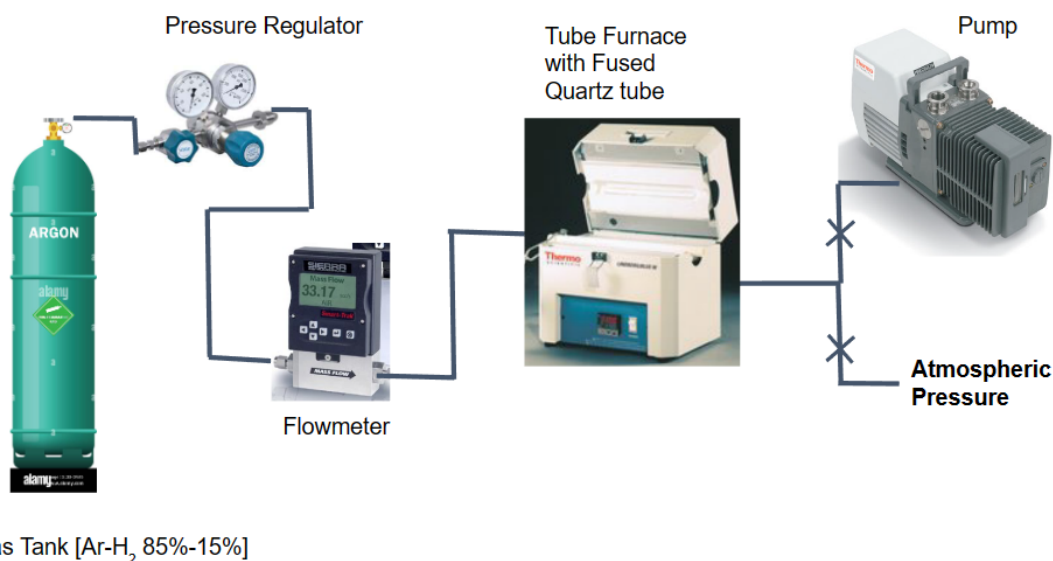


Figure 2.7: Scheme of the setup for the Carbonization and Graphitization annealing phases.

During the graphitization phase the amorphous carbon structure undergoes a rearrangement of carbon atoms, leading to the formation of graphitic layers. A deposition of a metal based solution is crucial to achieve lower graphitization temperature. Many aqueous solution of different concentrations of Na_2MoO_4 have been prepared for this step. A drop casting technique is used to deposit the metallic solution onto the carbonized sample. After loading again the sample in the furnace, the outlet is switched to the atmospheric pressure and a flow of 50 sccm is set. The temperature is set to 1090°C with a ramp-up of 20°C and kept for 10 minutes (for a total of 58 minutes considering the ramp-up). At the conclusion of the graphitization, the system is allowed to cool naturally, the sample is unloaded and checked under an optical and Horiba Xplora micro-Raman system (with a 532 nm laser) microscope.

During the test phase, most of the graphitization parameters have been investigated and tuned together with other fabrication parameters. To start, from the Raman microscope no graphitization was appreciable when using the Na_2MoO_4 solutions, so another set of solutions of $FeCl_2$ in IPA was used instead. In order to make the experiments more repeatable, the deposition process was changed employing a dummy sample which was vertically stacked above the actual sample, as similarly done in [21]. A visual reference is reported in Figure 2.8a. The dummy sample was placed in a piranha solution (3:1 ratio of sulfuric acid and hydrogen peroxide) on a hot plate (80°C) for 10 minutes for cleaning and surface activation purposes. Thereafter, a few drops of the iron solution were deposited on the dummy

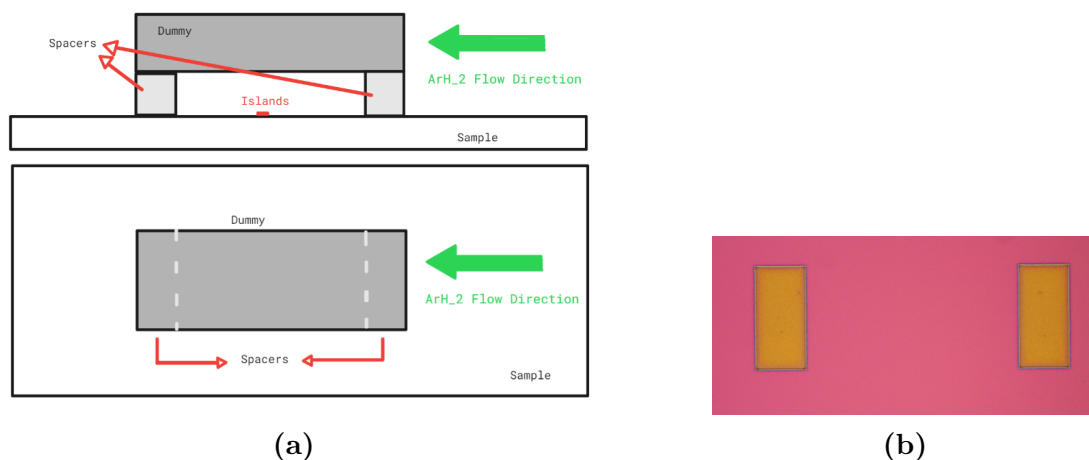


Figure 2.8: To the left is displayed the schematic of the vertical stack structure loaded in the furnace for the graphitization phase. To the right an optical image of the islands after being graphitized.

sample through spin coating, 1000 rounds per minute with an acceleration of 200 rps/s per 25 seconds.

2.3 Tuned parameters and Proof of Concept Experiments

Following a series of experiments, a baseline set of parameters for the graphitization of samples using iron aided graphitization has been established and documented. The determined parameters are provided in Table 2.2, serving as a reference for future graphitization processes. Notably, significant experiments were conducted comparing the optical images and Raman spectra of various samples, enabling the assessment of the parameter's influence (solution concentration, spacer thickness, graphitization time, ..) on sample morphology and its degree of graphitization. These findings shed light on the optimization of graphitization processes and contribute to the understanding of how specific parameters impact the structural characteristics of the samples. Note that all the Raman spectra reported in the following have been normalized respect to the G peak. Furthermore graphitizing samples utilizing the baseline parameters returns a uniform graphitization all over the sample surface.

The results of the effect of different iron chloride concentration in the deposited solution on the graphitic structure are reported in Figure 2.9. This experiment was performed with the following conditions: 30 minutes graphitization time, $250 \mu m$

FeCl ₂ Concentration (mM)	Spacer thickness (μm)	Temperature ($^{\circ}C$)	Time (no rump-up) (min)	Rump-up ($^{\circ}C/min$)	ArH ₂ Flow (sccm)
100	250	1090	30	20	50

Table 2.2: Reported the parameters used for the graphitization phase of the fabricated sensor. They represent the baseline for the investigation of the parameters presented in this section.

spacer thickness, 1090 $^{\circ}C$ temperature, 50 sccm flow, atmospheric pressure. It is possible to see how for higher concentrations of the solution, the D peak lowers indicating an higher graphitization degree, while the 2D peak becomes higher indicating a major quantity of layered graphene sheets. For higher concentrations the peaks are narrower indicating less interference of the sp^2 bonds over the sp^3 bonds. In Figure 2.10 the effect of different graphitization times is shown. This experiment was performed with the following conditions: solutions of 100 mM, 250 μm spacer thickness, 1090 $^{\circ}C$ temperature, 50 sccm flow, atmospheric pressure. The results indicate similar results as for the previous test, higher time leads to higher quality even if the two curves for 30 and 60 minutes show few to no differences, suggesting that after a certain threshold the effect of the time plays little to no role. The results on the effect of the flow are reported in Figure 2.11 which was performed at 50 mM of solution concentration, 250 μm spacer thickness, 1090 $^{\circ}C$ temperature, 30 minutes graphitization time, atmospheric pressure. Comparing the Raman spectra at different flows, is neither possible to define a linear nor monotonic trend. Even so, the measured curve of the sample fabricated with the lower flow posses the higher quality. In Figure 2.12 the effect of different spacer's thickness is shown. This experiment was performed with the following conditions: solutions of 1 mM still deposited through drop casting techniques, 10 minutes graphitization time, 1090 $^{\circ}C$ temperature, 50 sccm flow, atmospheric pressure. The results indicate that, in general, for direct to low thickness spacers the peaks are narrower and the 2D peak is higher, however a linear trend is not found implying the possibility that some other not considered parameter is playing a major role.

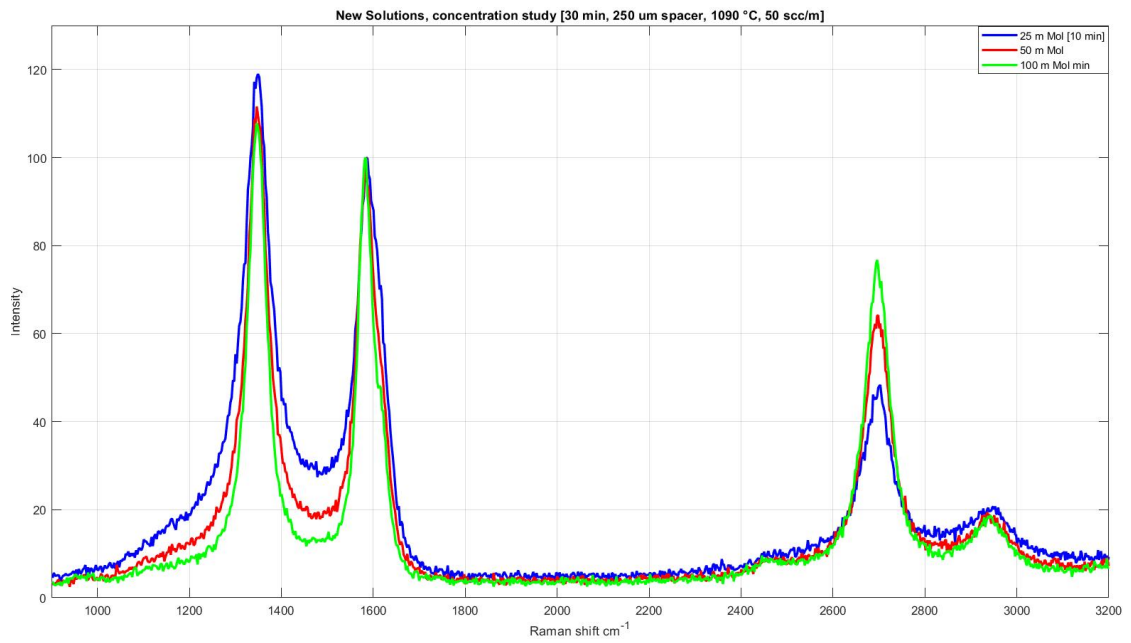


Figure 2.9: Effect of the different concentration of the iron chloride solution on the Raman spectrum.

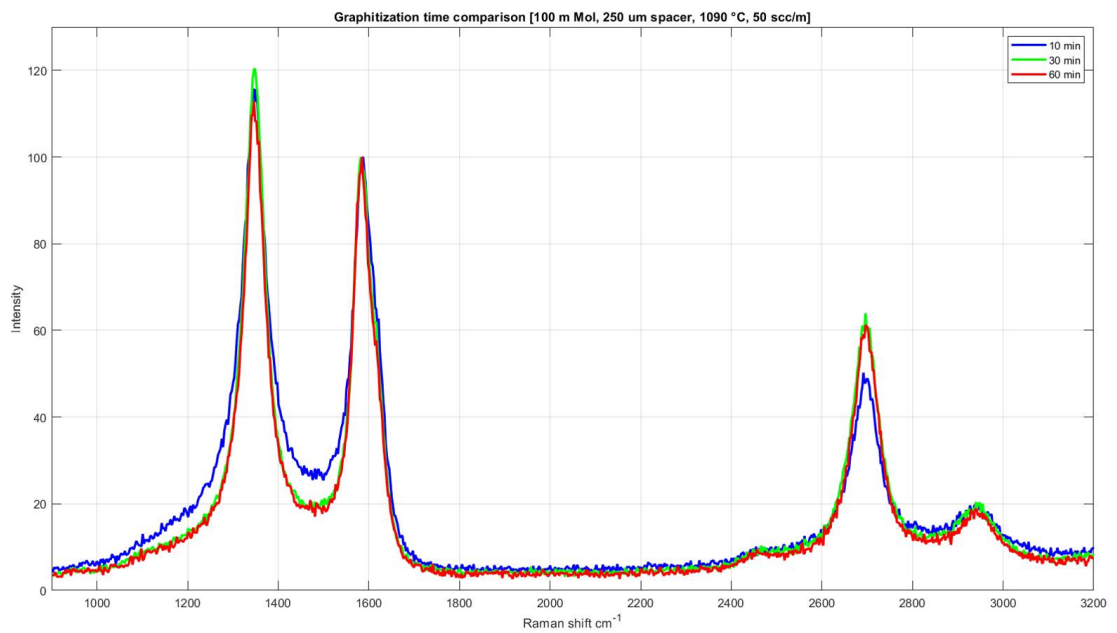


Figure 2.10: Effect of graphitization time on the Raman spectrum.

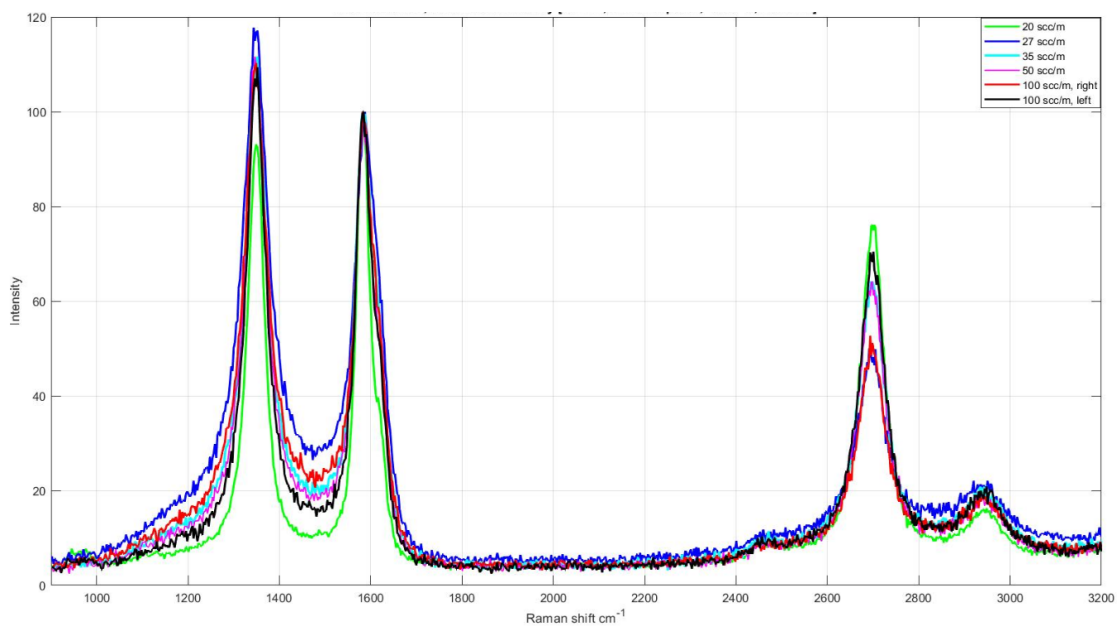


Figure 2.11: Effect of the Argon-Hydrogen flow on the Raman spectrum.

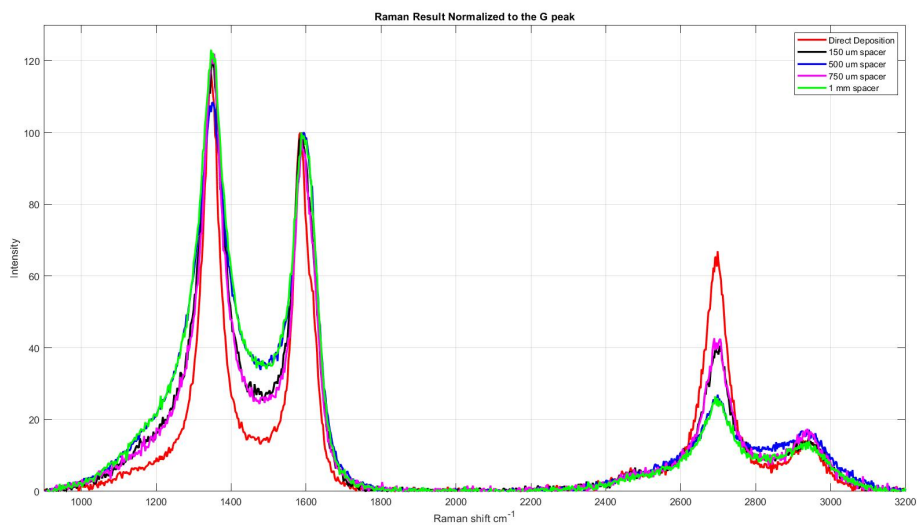


Figure 2.12: Effect of the spacers thickness on the Raman spectrum.

The results on the effect of the internal pressure of the furnace during the graphitization step are reported in Figure 2.13 which was performed at 50 mM of solution concentration, 250 μm spacer thickness, 1090°C temperature, 30 minutes graphitization time, 50 sccm flow. As displayed in the figure the over pressure

curve presents a higher D peak and narrower peaks respect to the other cases but it also presents a slightly lower 2D peak. The sample fabricated at over pressure looks optically less uniform and in some points is over etched as it is possible to see from the pink curve (the lower peak to the left states the presence of the SiO_2). A better trade-off for the pressure parameter is the curve at atmospheric pressure.

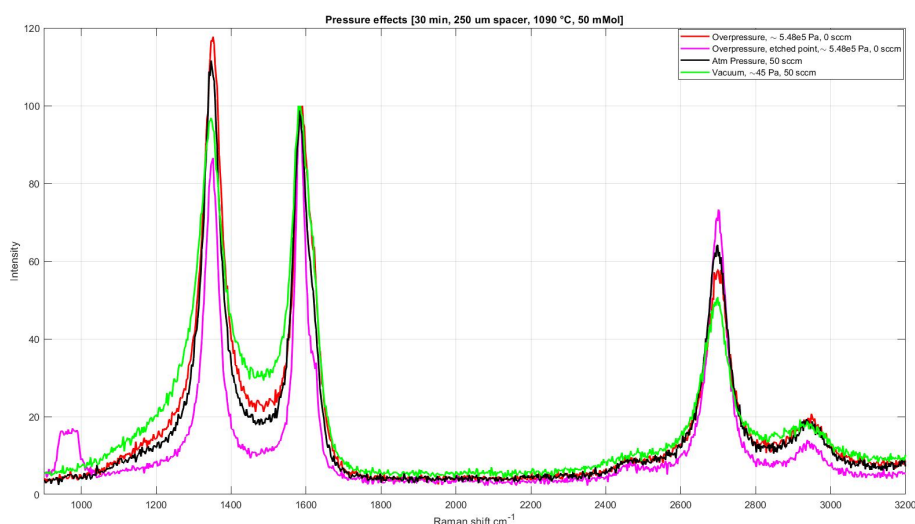


Figure 2.13: Effect of the internal pressure of the furnace on the Raman spectrum.

2.4 FSCV Setup and Measurements

2.4.1 Setup Description

Figure 2.14a depicts the arrangement of the in-vitro measurement setup, encompassing a flow chamber, a Fusion 4000 Syringe Pump by chemyx, the interface electronics board referred as board 2 described in the following chapter and an external computer. To deliver bio-analytes, a tailor-made microfluidic chamber was employed, featuring a Y-shaped configuration with two inlets, one outlet, and an incorporated Ag/AgCl reference electrode (see Figure 2.14b). Due to the low currents exhibited by the micro-sensors, a two-electrode measurement scheme has been utilized for voltammetry measurements. MA-8005 micromanipulator probes by SemiProbe were utilized to establish connections between the NG micro-sensors and the detection IC. The hole system was inside a Faraday cage in order to avoid unnecessary noise from the environment. Data acquisition and analysis were facilitated by a custom-made user interface program developed in MATLAB. In the

in-vitro experiments, NG micro-sensors with geometric areas of 360 and 580 μm^2 were employed. The PBS has been used as the buffer medium to deliver dopamine to the sensors. The PBS solution (1X concentration, pH of 7.4) was prepared by dissolving 8g of sodium chloride, 1.44g of sodium phosphate dibasic, 240 mg of potassium phosphate monobasic and 200 mg of potassium chloride per liter of de-ionized water. A dopamine solution of 2 mM concentration was prepared by dissolving dopamine hydrochloride powder in the previously prepared PBS solution and then diluted until a final concentration of 500 nM was reached. The solution was kept at 4°C and the syringe containing the dopamine solution in the pump was covered with cold thermal gel during FSCV experiments.

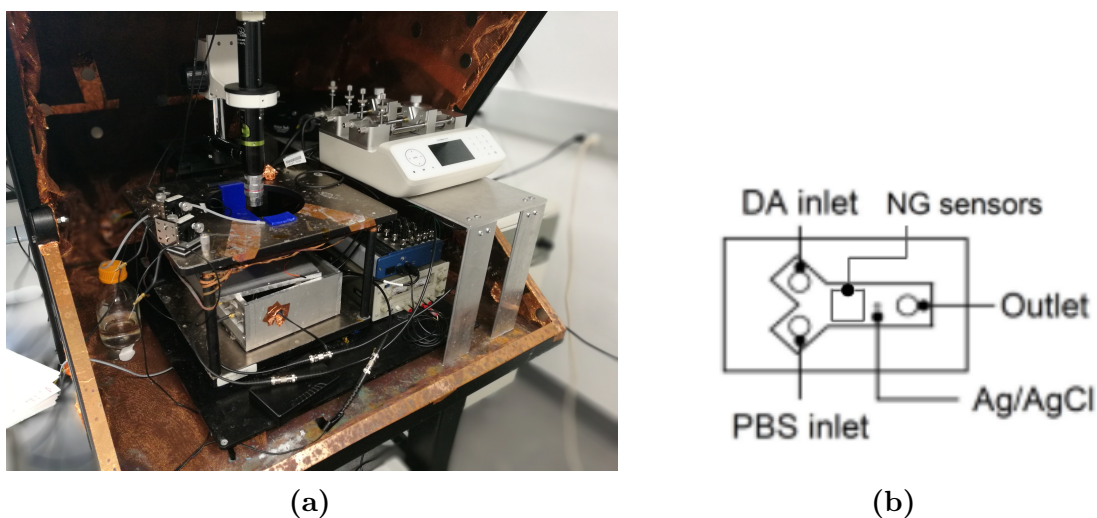


Figure 2.14: To the left is reported a photograph of the in-vitro measurement setup, to the right a scheme of the y-shaped microfluidic chamber. (b) is reprinted from [10].

2.4.2 Conditioning

The conditioning is a particular phase that the sensor must undergo in order to obtain stable voltammetry graphs. In this step the PBS solution flows through the microfluidic chamber while to the sensor a triangular wave (60 Hz, LPL -0.4, UPL 1.3 V, $\nu = 400$ V/s) is applied setting the parameters from the program interface. The combination of the PBS environment and high scan rate starts an electrochemical etching of the amorphous carbon of the NG sensors. When the measured current from the FSCV remains stable for a reasonable amount of time (5 minutes) the conditioning phase can be considered concluded; it may take from 1 to 2 hours. The measurements will be done with an N-shape signal (10 Hz, LPL

= -0.2, UPL = 0.6 ν = 200 V/s) with lower frequency so that the effect of the electrochemical etching can be neglected. In Figure 2.15 the Raman spectra of two sensors that underwent conditioning are compared with the sensor after being graphitized. Note that the *NGFe25* sample, whose graphitization is depicted as a blue line, is the sensor *FeCl3* before undergoing conditioning. We note that after conditioning the D peak is lower, the D and G peaks are narrower and the 2D peak is higher. Further information about the sensors structure after this stage are reported in the final section of this chapter.

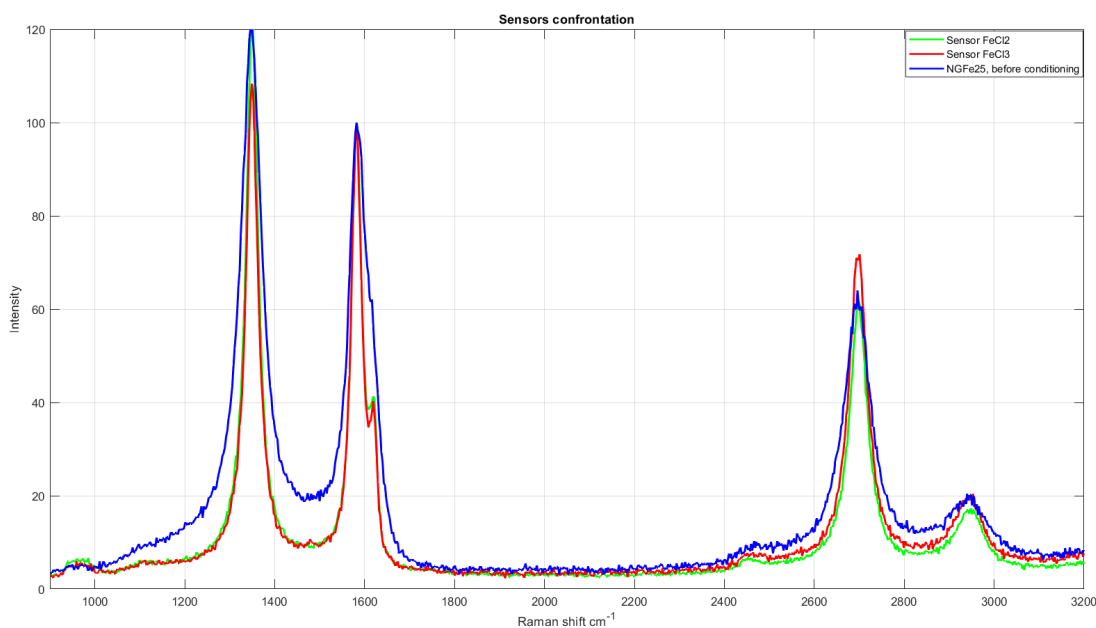


Figure 2.15: Confrontation of the Raman spectrum before and after the conditioning phase.

2.4.3 Results

In this section the results of the FSCV of a NG sensor fabricated following the parameters in Table 2.2 are reported. In Figure 2.16 the CV graphs of the sensor are reported; Figure 2.16a shows the complete voltammogram of the sensor for an applied N-shaped wave when in the flow chamber only the PBS solution is flowing and when the solution with dopamine (500 nM) is flowing. In this way, the background signals and the signals from the PBS solution can be recorded and then its average can be subtracted from the measurements while detecting dopamine. In this way Figure 2.16b is obtained. The extracted positions of the oxidation and reduction peaks are 0.28 V and -0.002 V respectively.

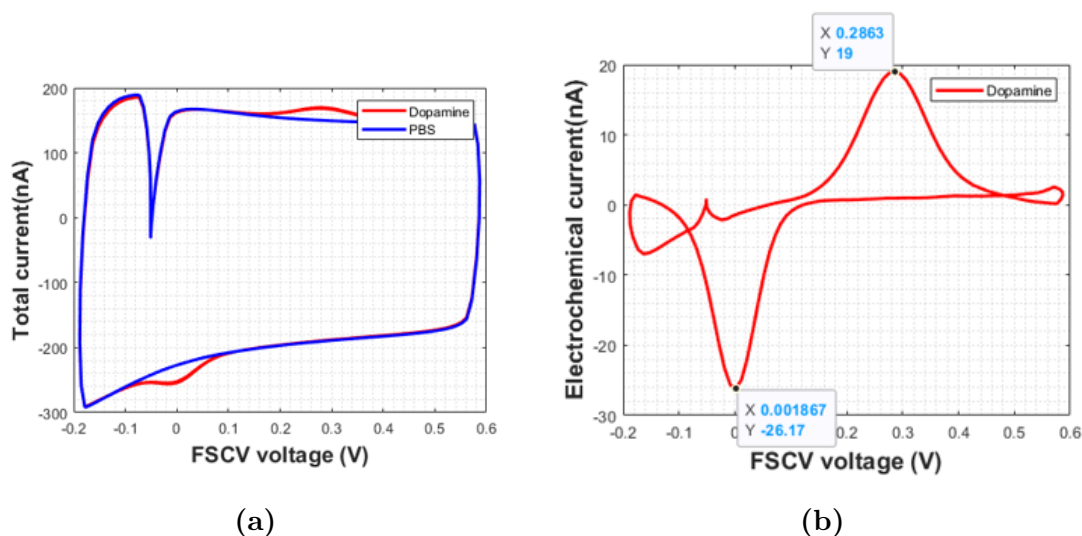


Figure 2.16: (a) Voltammograms obtained during the detection of dopamine and during the detection of PBS only. (b) Resulting CV of the dopamine detection after the removal of the background signal.

The dependence of the current of the oxidation and reduction peaks from the maximum applied voltage has also been investigated. More FSCV experiments have been performed varying the UPL of the N-shaped input wave from 0.6 V to 0.8 V and 1 V. Results are displayed in Figure 2.17, especially the dependence of the reduction peak current in Figure 2.17a and for the oxidation peak current in Figure 2.17b. As we can see, for higher maximum voltages the module of the current lowers revealing a linear trend.

2.5 AFM and SEM images

The NG sensors used for the FSCV measurements have been analyzed by means of AFM and SEM, in order to further investigate their structure and morphology. In Figure 2.18 the AFM images and the related measured profile taken from the actual sensor and its sister island are shown. The sister island exhibited a measured mean roughness of 3 nm, whereas the actual sensor displayed a higher value of 13 nm. Furthermore, the sister island had a measured height of approximately 106 nm, while the sensor's height ranged from 40 to 50 nm. Considering the sensor surface, holes around 30 nm profound can be seen even though the the material does not seem porous. These measurements indicate differences in surface roughness and height between the sister island and the sensor, highlighting variations in their morphological characteristics. It is assumed that too much amorphous carbon

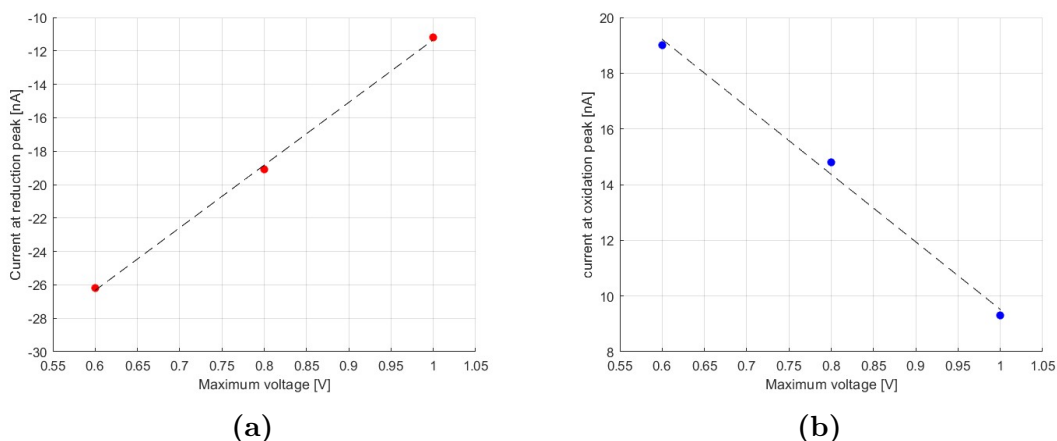


Figure 2.17: Voltage dependence of current at the reduction (a) and oxidation peak(b). The dashed line serves as a guide for the eye, representing the linear interpolation of the points.

deposited in split planes that after the electrochemical etching results in this structure. The SEM images of the sensor and its sister island are reported in

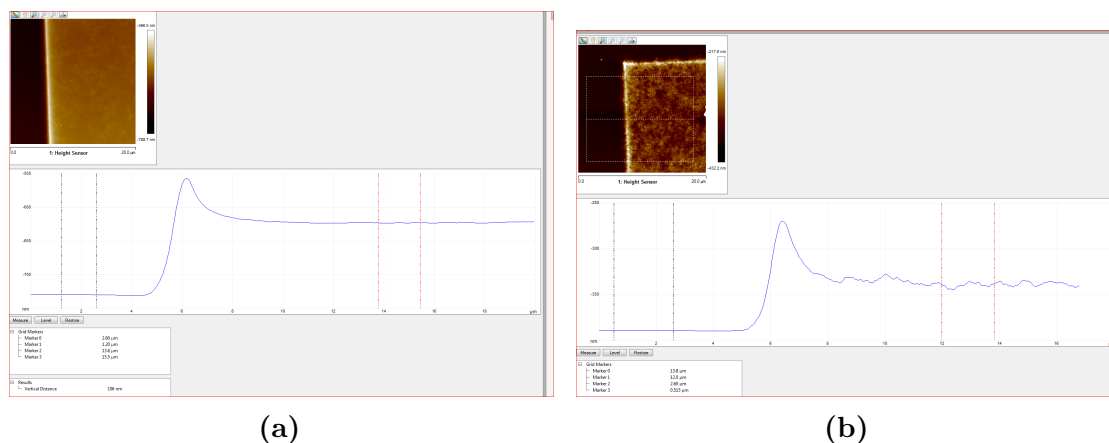


Figure 2.18: AFM images of the two sister islands and related measured profile. On the left the island that did not underwent conditioning is thicker respect to the one that did (right).

Figure 2.19. Upon comparing the two SEM images, a greater number of white residues can be observed on the sensor. The nature of these contaminants, whether they are iron or chloride residues from the previously deposited metallic solution or not, remains unclear. Further investigations should be done in the future to accurately identify and characterize these residues.

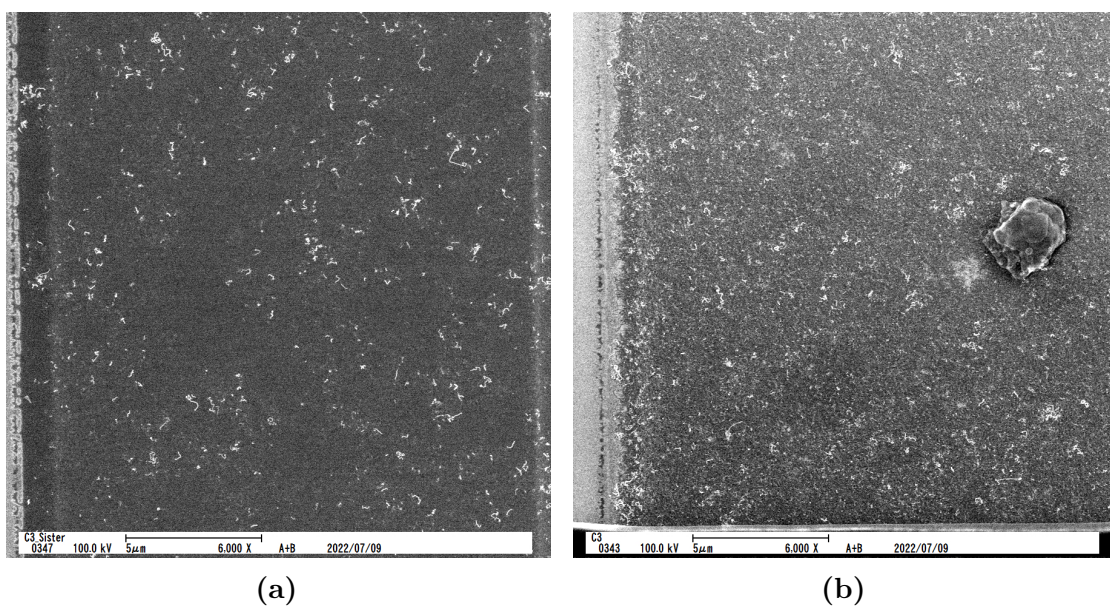


Figure 2.19: SEM image of the islands after the preliminar conditioning phase for FSCV measurements. To the left is reported the sister island which has not undergone conditioning while on the right the tested island.

Chapter 3

Detection Circuitry

3.1 Theoretical introduction

Noise is a pervasive challenge in electronic circuits, posing significant implications for system performance and signal integrity. In this context, special attention is devoted to the SNDR, a key parameter that characterizes the quality of an electronic system's output signal in relation to the noise and distortion components. In Addition an algorithm for evaluating the PSD and estimating the voltage noise of the system will be presented. Finally, we delve into the crucial aspects of PCB design and offer practical tips for achieving low-noise designs.

3.1.1 Noise and Signal to Noise and Distortion Ratio

In electronics, noise refers to any unwanted or random fluctuations or disturbances in an electrical signal. It manifests as additional signals or variations superimposed on the desired signal, making it difficult to accurately extract or interpret the intended information. Noise can arise from various sources, such as thermal effects, electromagnetic interference, and electronic component imperfections, and it can impact the overall performance and reliability of electronic systems.

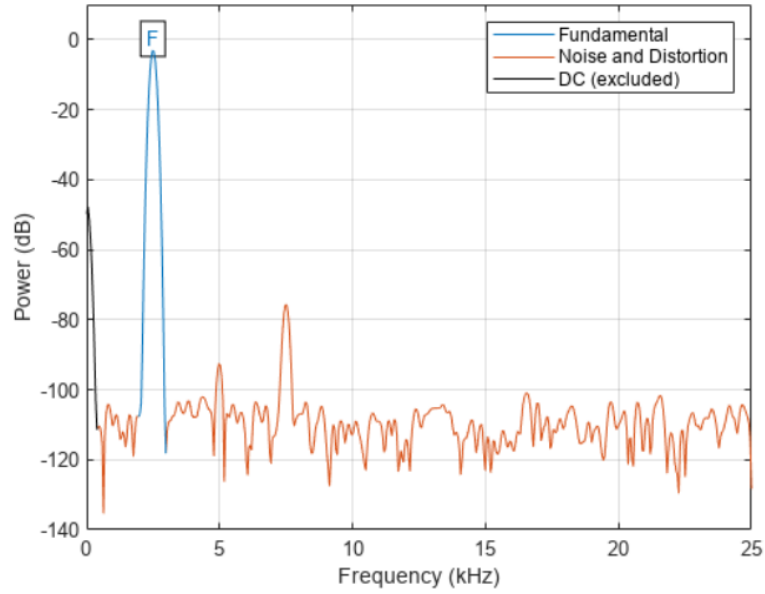


Figure 3.1: Representation of the power spectrum of a reference signal. In blue the power of the frequency carrying the signal is reported, while in red the noise plus distortion contribution are represented. Reprinted from [22].

In electronics, SNDR, also called SINAD, is a measure of the quality of an analog-to-digital or digital-to-analog conversion process. SNDR quantifies the ratio between the amplitude of the desired signal and the combined effects of noise and distortion present in the output signal. It provides a quantitative assessment of the system’s ability to accurately capture and reproduce the desired signal while minimizing the impact of unwanted noise and distortion components. A higher SNDR value indicates better signal fidelity and improved system performance.

$$SNDR = 20\log\left(\frac{S}{N + D}\right) \quad (3.1)$$

Where S represents the power of the signal at a discrete frequency component, N represents the power of the noise distributed over the rest of the spectrum, and D represents the power of the Total Harmonic Distortion (THD) components with a frequency that is a positive integer multiple of the fundamental frequency of the signal.

3.1.2 Power Spectral Density and Integrated Voltage Noise

The PSD is a widely utilized tool for analyzing and characterizing random processes in electronic and telecommunication systems. One common application of the PSD

is to quantify and understand the noise present in a system. By examining the PSD, it is possible to determine the power of the noise, which in turn enables the evaluation of the system's SNDR [23]. This information is crucial for assessing the performance and reliability of electronic and telecommunication systems, allowing for the optimization of signal quality and the mitigation of unwanted noise interference.

Let us consider any measured time discrete voltage signal, that is a vector in the form:

$$V(t) = [V_{t_1} V_{t_2} \dots V_{t_N}] \quad (3.2)$$

The first step is to calculate the PSD is to remove the DC component (mean) of the signal and calculate its Discrete Fourier Transform (DFT). In order to do so, usually the Fast Fourier Transform (FFT) algorithm is utilized.

$$\begin{cases} DFT = FFT(V(t) - V_{mean}) \\ V_{mean} = \frac{1}{N} \sum_{i=1}^N V_i \end{cases} \quad (3.3)$$

Generally the result of the FFT is defined in a domain spacing from $-F_{Nyquist}/2$ to $F_{Nyquist}/2$, so the spectra includes positive and negative frequencies as shown in Figure 3.2 (negative frequencies are the complex conjugates of the positive frequencies). Negative frequencies are not needed for the PSD calculation, so they are usually removed with the following transformation:

$$DFT = DFT\left(1 : \frac{N}{2} + 1\right) \quad (3.4)$$

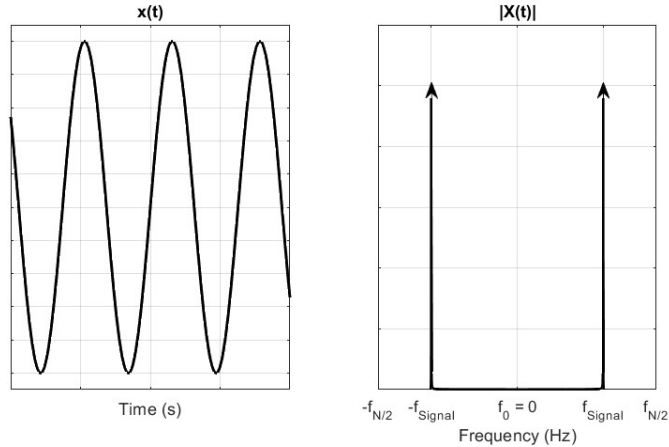


Figure 3.2: Representation of a sinusoidal signal in time domain on the left and its resultant FFT on the right. Because negative frequencies are not physically measured, DFT is usually redefined only between 0 and half the Nyquist frequency.

The next step to obtain the PSD is to take the module of the DFT and square it so that we pass from the signal (voltage) domain to the power domain. In order to maintain physical meaning a normalization factor should also be taken into account, therefore the transformation becomes:

$$PSD = \frac{N}{F_S} |DFT|^2 \quad (3.5)$$

Note that the N term refers to the total number of samples of the vector $V(t)$ while the F_S term corresponds to the sampling frequency at which the signal has been digitized. The normalization constant, $\frac{N}{F_S}$, corresponds to the total time window in which the signal was sampled.

Finally, we should account for the energy lost in removing the negative portion of the spectra multiplying the remaining frequencies by 2. The 0Hz and half Nyquist frequency results don't have an imaginary component and are not included in the negative frequency side, so they remain unchanged.

$$PSD(2 : end - 1) = 2 * PSD(2 : end - 1) \quad (3.6)$$

Sometimes it can be useful to express the noise through the Integrated Voltage Noise that refers to the cumulative effect of voltage fluctuations or random variations in an electronic system over a given frequency range. Integrated voltage noise is typically expressed as the root mean square (RMS) value of the voltage noise integrated over a specified frequency bandwidth. As above mentioned the integration is done over a frequency range, which introduces the need to define the frequency vector associated to our PSD:

$$f = \frac{F_S}{N} * \left(0 : \frac{N}{2}\right) \quad (3.7)$$

At last, the Integrated Voltage Noise is obtained with the following:

$$V_{n,RMS} = \sqrt{\frac{BW}{N_{BW}} \sum_{i=1}^{N_{BW}} PSD_i} \quad (3.8)$$

where the definition $BW = f(N_{BW})$ has been used.

3.1.3 PCB Design

PCB design plays a critical role in modern electronics, providing a platform for interconnecting and supporting electronic components. It involves the layout and optimization of conductive pathways, signal traces, power planes, and component placement on a board to ensure efficient and reliable electrical connections. PCB

design encompasses various considerations such as signal integrity, power distribution, thermal management, manufacturability, and electromagnetic compatibility. By employing advanced design tools and adhering to industry standards, engineers can create PCBs that meet the specific requirements of electronic systems, enabling efficient signal transmission, minimized noise, and optimal performance. In the following the main steps, from the circuit determination to the PCB fabrication and assembly are briefly covered.

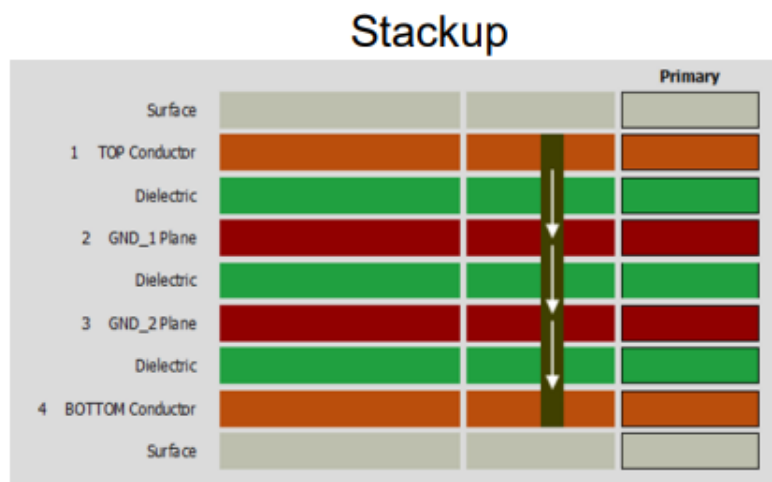


Figure 3.3: Representation of the stackup of a general PCB. The stackup consists of alternating conductor and dielectric planes; usually the external conducting planes are used for the signal part while the internal ones are reserved for ground. Particular cases and more complicated stackup structures may be different.

CAD tools are essential for PCB design, enabling designers to create and visualize complex PCB layouts in a virtual environment and providing libraries of components, footprints, and symbols, saving valuable time. For the boards realization the OrCAD software has been employed and [24] has been used for reference. In the initial non-software phase, circuit functionalities must be defined based on specific requirements and applications. Simulations are executed to validate the circuit design, and component verification is carried out to ensure the availability of selected components in the market. Footprint research is conducted to determine the appropriate package and pin layout for each component.

Moving into the PCB software phase, the geometry of the final board is defined, including its dimensions and shape. The stackup (Figure 3.3), which determines the arrangement of various PCB layers, and the design rules, such as spacing between signal traces and structure of power planes, have to be established. In the next phase components are placed strategically on the board, considering factors

like signal integrity, thermal management, and manufacturability. Routing is then performed to create the necessary connections between components, ensuring proper signal flow and avoiding interference; a visual reference is reported in Figure 3.4. Finally, the manufacturing files, including Gerber files, are generated and provided to the manufacturer.

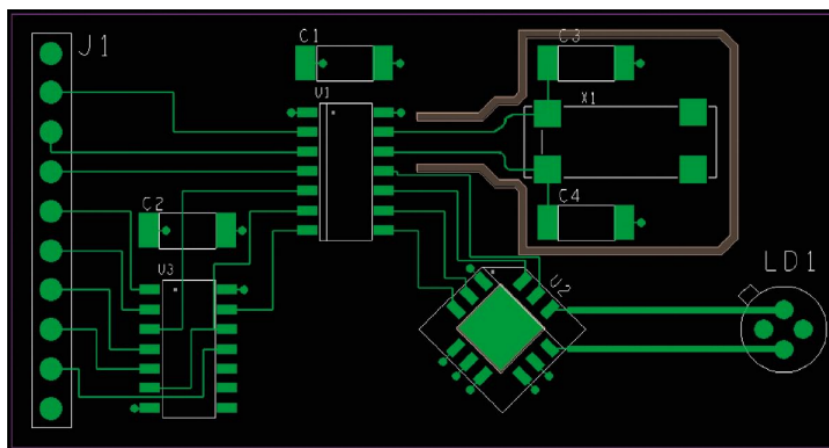


Figure 3.4: Board design after completing the routing step. It is possible to see how the footprints of every component presents metal leads that will be connected through routes. Reprinted from [24].

Once the manufacturer has fabricated the board, and all the components have been purchased, the PCB assembly can start. Surface mount and through-hole components needs different assembly techniques. Surface mount components are attached using the reflow soldering technique, where solder paste is applied to the board, the components are placed accurately, see Figure 3.5. The board is then heated in an oven to melt the solder paste and create secure electrical connections. On the other hand, through-hole components are soldered using iron soldering techniques, where solder wire and a heated soldering iron are used to establish connections between component leads and the board. Both techniques ensure reliable and robust connections, allowing the PCB to function as intended.

3.2 Project Parameters and Concepts to Select an ADC

When designing a circuit for detection purposes, it is crucial to define the parameters in a way that allows the digital part to detect a signal limit effectively while minimizing the impact of noise from the analog front end. Here are some considerations:

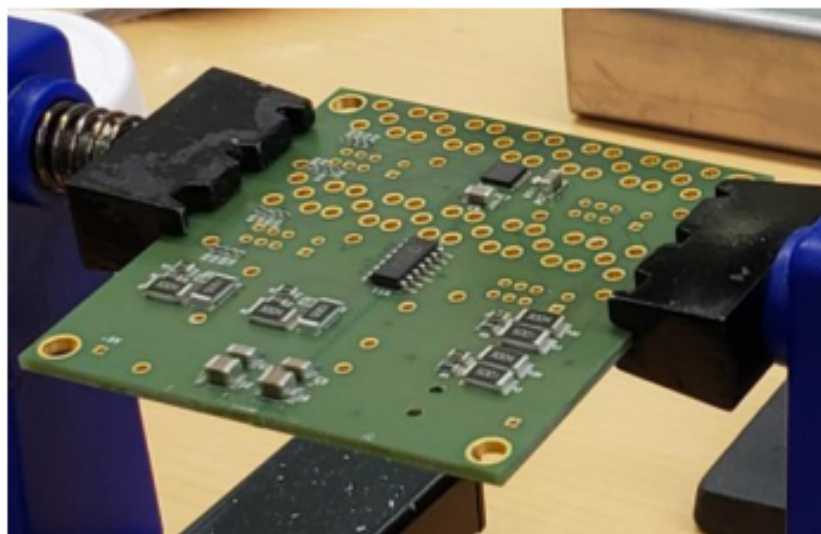


Figure 3.5: Last phase of the PCB production: component placement and soldering.

- SNDR: Determine the required SNDR for accurate detection. Setting a suitable SNDR threshold ensures that the digital part can detect signals above the noise floor without being overly sensitive to noise variations.
- AFE Design: Design the AFE to have low noise and high linearity. Use low-noise components, proper grounding techniques, and appropriate filtering to minimize the noise contribution from the analog stage. The AFE should provide sufficient gain to amplify the signal above the noise level without introducing significant distortion.
- Bandwidth: Define the bandwidth of the AFE based on the frequency range of the desired signals. By limiting the bandwidth to the relevant frequencies, you can minimize the impact of out-of-band noise on the detection process.
- Filtering and Anti-Aliasing: Employ effective filtering and anti-aliasing techniques to remove unwanted noise and prevent aliasing artifacts.
- ADC Resolution and Sampling Rate: Select an ADC with adequate resolution and sampling rate to capture and digitize the amplified signal accurately. Higher resolution enables finer quantization levels, while a sufficient sampling rate ensures faithful representation of the analog signal in the digital domain.

The project parameters for our project are reported in the following:

- $\text{SNDR} \geq 80$

- Input Voltage Range of 3.3V
- Possibility of reading from more sensors (multichannel)
- Considered Bandwidth of 5 kHz
- Minimum Sampling Rate of 20 kHz

ADCs are essential for converting continuous analog signals into discrete digital representations, serving as vital interfaces between analog and digital domains. They enable processing, storage, and analysis of real-world signals in digital systems. Widely used in telecommunications, data acquisition, audio processing, sensor networks, and control systems, ADCs offer advantages such as accurate sampling, improved signal fidelity, noise reduction, and compatibility with digital signal processing algorithms.

When it comes to pick an ADC, a useful parameter to define is Effective Number of Bits (ENOB). ENOB represents the actual resolution of an ADC converter, indicating the number of bits that contribute to its precision; it is strictly related to the SNDR. The formula for calculating the exact ENOB given the SNDR and the input amplitude of the signal is reported in the following [25].

$$ENOB = \frac{SINAD_{Measurd} - 1.76dB + 20\log\left(\frac{FullscaleAmplitude}{InputAmplitude}\right)}{6.02} \quad (3.9)$$

As already stated, the minimum SNDR needed for dopamine detection is 80 dB, supposing to read a signal whose input amplitude is equal to the full scale amplitude, an ENOB of 13 is obtained. So, when looking for an ADC, it is fundamentally important to evaluate its quantization noise and performance through the SNDR or its digital counterpart, the ENOB.

3.3 Description of the First Board

The first board realized to test and develop the AFE that will be interfaced with the NG sensor, is composed of four different channels that are mainly divided in two designs. The objective of the design is to keep the noise in the circuit as low as possible to detect dopamine with the highest sensibility. This two designs are mostly similar, except for the differential amplifier element which is a Programmable Gain Amplifier (PGA) for the first two channels and a Instrumentation Amplifier (IN-AMP) for the last two. A detailed composition of the fundamental blocks making up the four channels is reported in Table 3.1, the circuit schematics of channel 1 and 3 are respectively reported in Figure 3.6 and Figure 3.7.

The board is designed to amplify a current signal obtained from the NG sensor and a dummy sensor using a Trans Impedance Amplifier (TIA). The purpose of

Channel	Current Amp.	Differential Amp.	Filters	Others
1	TIA	PGA	LP (1 st)	Switches for T.P.
2	TIA	PGA	LP (1 st)	/
3	TIA	IN-AMP	LP-HP (2 nd)	Switches for T.P.
4	TIA	IN-AMP	LP-HP (2 nd)	/

Table 3.1: Description of the fundamental blocks constituting the 4 channels of the first board. All the filters reported in the table are active filters. Note T.P. stands for testing points.

the dummy sensor is to read the environmental noise and so, is physically close to the NG sensor. The TIA converts the current signal into a corresponding voltage signal, amplifying it for further processing. The amplified signal from the two sensors is then subtracted to eliminate the environmental noise component from the dopamine readings, leaving behind a "cleaner" signal from the sensor. This subtraction process is executed with a PGA or with a IN-AMP, depending on the channel. Final Low Pass (LP) and High Pass (HP) filtering stages are added to remove lower/higher noise frequencies. Switches for the testing points, which are practically implemented with simple buffers, have been added to test if their presence may lower the noise at the output of the channel. The basic elements constituting the channels will be deepened in the following paragraphs.

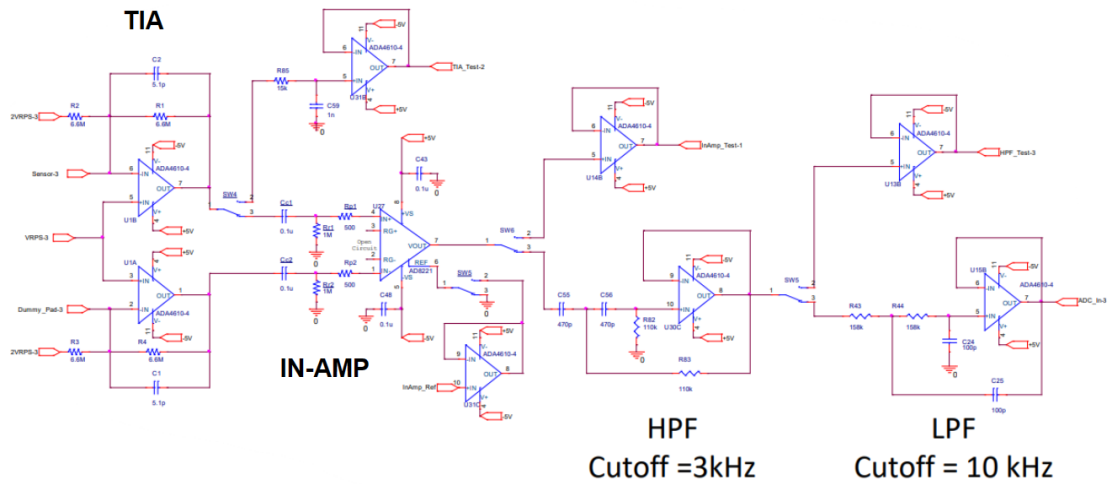


Figure 3.7: Third channel of the Board composed by a TIA stage plus an IN-AMP stage. A test point has been added after the TIA, IN-AMP and HPF to verify the signal during the testing phase. The circuit final part is a second order HPF followed by a second order LPF.

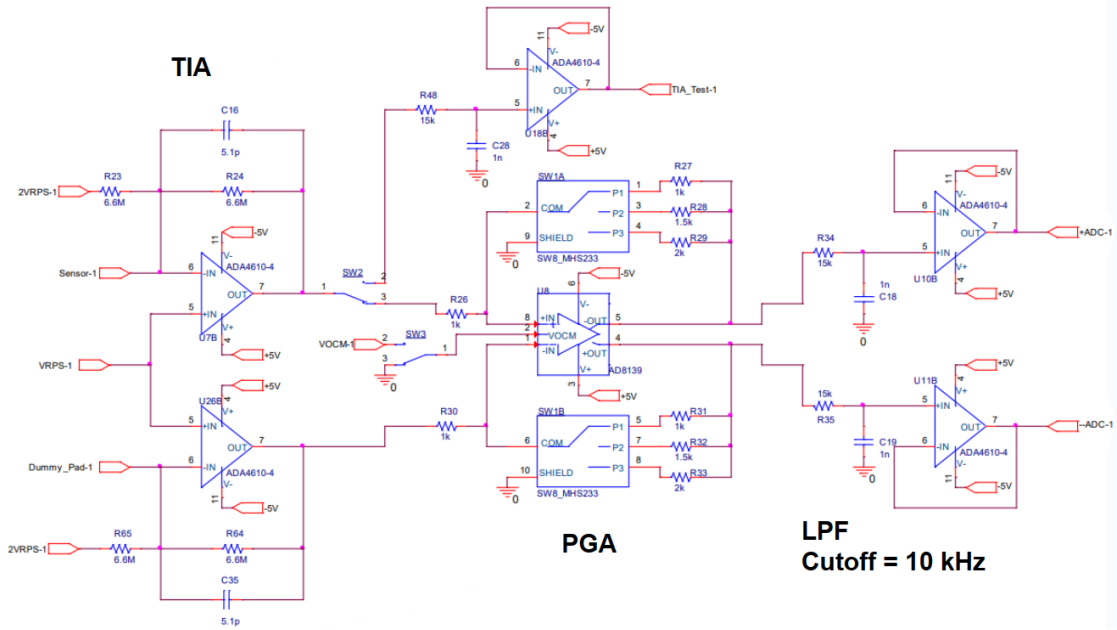


Figure 3.6: First channel of the Board composed by a TIA stage plus a PGA stage. A test point has been added after the TIA to verify the signal during the testing phase. The circuit final part is a first order active LPF.

3.3.1 Trans Impedance Amplifier stage

The TIA is a fundamental building block in many electronic systems, particularly in applications involving the detection and amplification of current signals. As the name suggests, a TIA converts an input current into a corresponding output voltage. This amplifier configuration is widely used in various fields such as optical communications, photodetection, sensor interfaces, and biomedical instrumentation. The TIA offers several advantages, including high input impedance, low noise, and wide bandwidth, making it suitable for capturing weak current signals and providing accurate and reliable amplification. To be precise the TIA employed is a R-TIA or resistive TIA, not to be confused with the capacitive TIA. The R-TIA consists of an Operational Amplifier (Op-Amp) and a feedback resistance R_F , which defines the transimpedance (gain) of the system. However, due to the parasitic capacitance C_P at the input of the amplifier, a feedback capacitor C_F needs to be introduced to ensure the stability of the TIA [26]. A schematic of the block is shown in Figure 3.8.

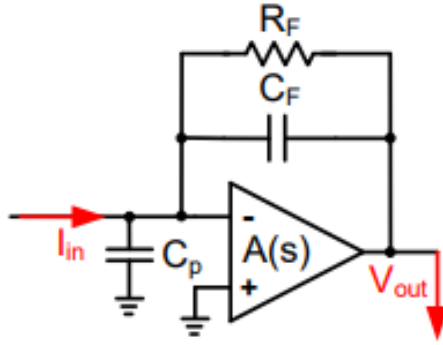


Figure 3.8: Schematics representing the R-TIA module. Reprinted from [26].

As we can see from the CV graphs from [10], the maximum output current from the NG sensors is around ± 250 nA. Between most of the ADCs a common value for the full scale range is $3.3V$; considering this value as our maximum voltage to be digitized, the value of the feedback resistance can be found. For this project a feedback resistor of $6.6M\Omega$ has been selected, giving a maximum voltage output of $\pm 1.65V$. Finally, the Feedback Capacitance can be calculated from [27], through the following formula:

$$C_F = \frac{1}{4\pi R_F GBP} * [1 + \sqrt{1 + 8\pi R_F C_P GBP}] \quad (3.10)$$

where GBP represents the Gain Bandwidth Product of the selected op-amp and the parasitic capacitance has been approximated as 580 pF. Doing the calculation, which may differ for different Op-Amp, we obtain a capacitance of a few pF; a final C_F of 5.1 pF has been selected.

3.3.2 Programmable Gain Amplifier stage

The PGA is a key component in electronic systems for which flexible and adjustable amplification capabilities are essential. It provides the ability to modify the gain of the amplifier circuit according to specific application requirements, making it a versatile tool in fields such as audio processing, instrumentation, communications, and sensor interfaces. In particular, the PGA structure utilized is the Variable Impedance PGA where a few discrete gain values can be selected through a control element (switch) so that the value of the equivalent resistor may be changed [28]. A visual reference is reported in Figure 3.9b. The PGA is implemented utilizing a Fully Differential Amplifier (FDA) as its core, having 3 resistive elements per input, which allow 3 different gain selection: 1, 1.5 and 2. Using an FDA as the central element comes with many advantages:

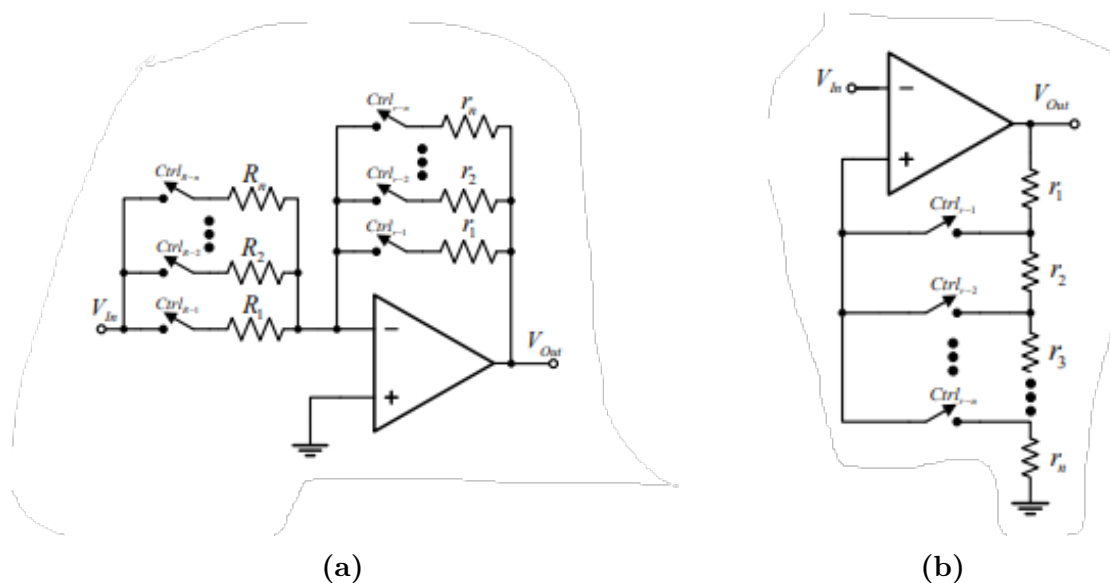


Figure 3.9: Resistor array PGA. Reprinted from [28].

- Amplifying only the difference between the two input voltages, the FDA effectively suppresses common-mode noise.
- Its differential architecture helps reduce the impact of external noise sources.
- It also rejects power supply noise, ensuring that it has minimal impact on the amplified output signal.

A part from its noise suppression/rejection, a differential output can help in shielding the signal while traveling from the AFE board to the board in which the ADC will be implemented.

3.3.3 Instrumentation Amplifier stage

The IN-AMP is a specialized operational amplifier-based circuit widely used in applications that demand accurate amplification of small differential signals in the presence of common-mode noise. It provides high gain, excellent common-mode rejection, and low input impedance, making it an essential component in precision measurement systems, medical instrumentation, sensor interfaces, and data acquisition systems. The IN-AMP unique architecture allows for the amplification of the voltage difference between two input signals while effectively rejecting any common-mode noise. Contrary to the Op-Amp, an IN-AMP employs an internal feedback resistor network that is isolated from its signal input terminals. When the signal is applied at the differential inputs, gain is present internally but

can also be selected externally by an external gain resistor (also isolated from the signal inputs) [29].

3.3.4 Filtering Stages

For the two PGA channels an active first order Low Pass Filter (LPF) with a cutoff frequency of 10 kHz has been added as final module, while for the two IN-AMP channels an active second order LPF and High Pass Filter (HPF) with a cutoff frequency of 10 kHz and 3 kHz respectively have been added as the final stages. The role of the filtering stages is to remove the noise from the bandwidth of our signal of interest. The amplifier prevents the load impedance of the following stage from affecting the characteristics of the filter. The two type of structures in the board present different order of filters because the objective of this board is to practically investigate the effects of different designs at the board level. The adding of the HPF in the IN-AMP channels is to verify if it can be used as a differentiator in order to remove the background current from the sensor which, at voltage level corresponding to the redox peaks of dopamine, is mostly an horizontal shift [Insert CV figure]. For testing purposes, the filtering stages have been modified at a board level for fairness. This implies removing or substituting the RC components of the HPF with 0Ω resistors making it a buffer, and demote the second order low pass to first order.

3.4 Tests on the First Board

The test setting of the board consists of a 782258-01 Data Acquisition System (DAQ) from National Instruments, a YB1206000-USB 12V/5V power bank from Talentcell, a computer equipped with LabVIEW to be interfaced with the DAQ and obviously our board made by off-the-shelves components. Tests are performed inside a Faraday cage, in order to avoid external environmental noise to affect the board. The stimuli to feed the board as well as the board outputs are handled by the DAQ, while the power bank is used as a clean power source to power the board in order to provide stable, low noise power. The output signals are stored in text files and analyzed with MATLAB at a later time. A visual reference of the setup is reported in Figure 3.10. A set of preliminary test has been performed to check the functionality and verify that the soldering phase has been well performed. In the following the results obtained for the noise performance of the signal generator (DAQ) and the board are presented.

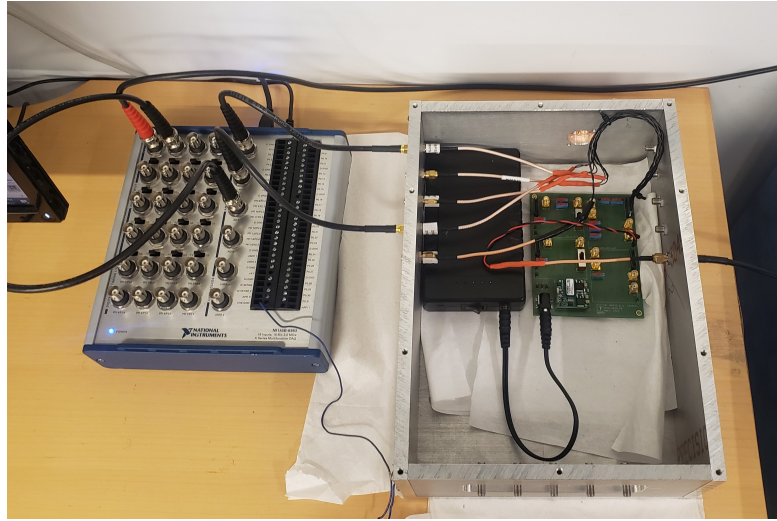


Figure 3.10: Photos of the noise test setup.

3.4.1 Signal Generator Noise Check

In Figure 3.11 and in Figure 3.12 the measured dynamic characteristics of the signal generator are shown. As we can see from the SNDR graph, at its maximum amplitude the DAQ has a SNDR higher than 80 dB, enough to detect a concentration of dopamine of about 10 nM [10]. The intersection of the linear interpolation with the x axis, namely when the SNDR is equal zero, represents the Signal to Noise Ratio (SNR) and may be considered as a double check of the quality of the generated/measured signal with the signal generator. Thanks to the previously reported algorithm for the estimation of the voltage noise, integrating the blue graph in Figure 3.12 a voltage noise of $21.6 \mu V_{RMS}$ is extracted.

3.4.2 Board Noise

As done in the above section, the PSD and the voltage noise resulting from its integration have been measured for all the channels. An example of the PSD for channel 1 is reported in Figure 3.12 while the resulting noise is reported in Table 3.2. Note that the last column of the table reports the Referred-to-input (RTI) current noise, obtained by dividing the output voltage noise by $6.6 M\Omega$, the transimpedance amplification of the first stage of the channel. This current is strictly related to the lowest limit of detection of dopamine from our sensor.

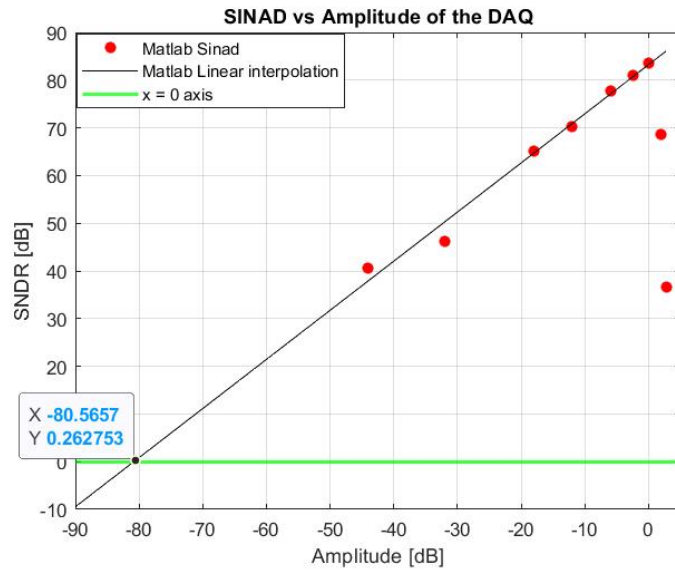


Figure 3.11: Variation of the SNDR of the measured signal in function of its amplitude. The crossing point on the x axis represents the maximum ratio between signal and noise, without taking into account the distortion.

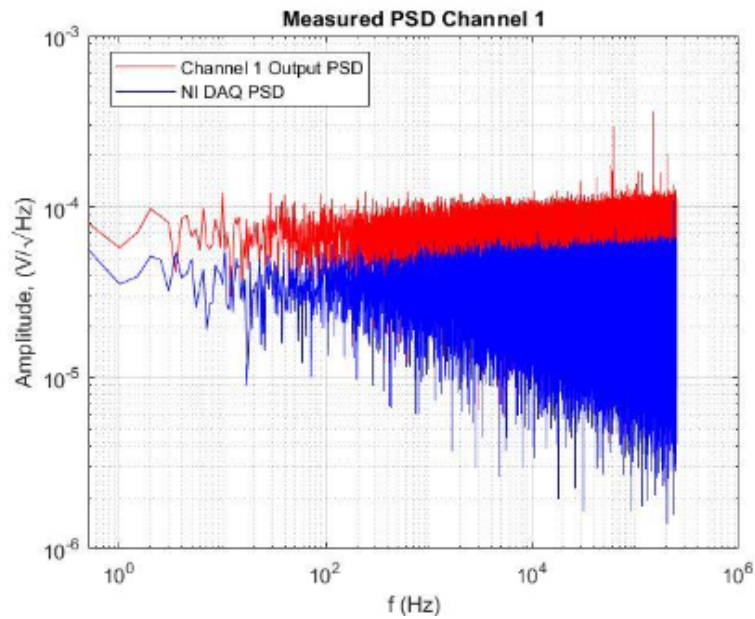


Figure 3.12: In blue is reported the PSD of the DAQ, while in red is reported the PSD of the total system (channel1 plus DAQ).

Channel	Integrated Noise (μV_{RMS})	RTI Noise (pA_{RMS}).
1	52.3	8.1
2	52.5	8.1
3	67.1	10.3
4	81.4	12.5

Table 3.2: Integrated noise over the interested bandwidth (0 to 5 kHz) in RMS values referred to the output voltage and reported to the input current for board 1.

3.5 Description of the Second Board

The second board is specialized for multichannel purposes and employs eight IN-AMP channels. The choice of the IN-AMP over the PGA as the differential element of the circuit is a consequence of practical issues in fact, due to the similar levels of noise measured for the two types of channels, the IN-AMP ones present a clear advantage: a lower number of outputs. It may seem trivial, but having to lead eight outputs from the board to the ADC instead of sixteen reduces the complexity of the board, its connections and their related issues. The circuit schematics is reported in Figure 3.13, the first two channels and the dummy pad buffer and TIA sections are displayed. The channels are identical to the IN-AMP channels of the previous board except for the final filtering stages, where the HPF is removed while the LPF is converted from active second order to active first order.

3.6 Test on the Second Board

The second board has undergone the same set of tests of the first board. The extracted noise results will be reported in the following subsection. As already done with the first board, the PSD and corresponding voltage noise were measured for all channels. Table 3.3 presents the resulting noise data. Notably, the last column of the table indicates the Referred-to-Input (RTI) current noise, calculated by dividing the output voltage noise by $6.6M \Omega$, which represents the trans-impedance amplification of the initial stage of the channel. This current measurement is directly associated with the lower limit of dopamine detection achievable by our sensor.

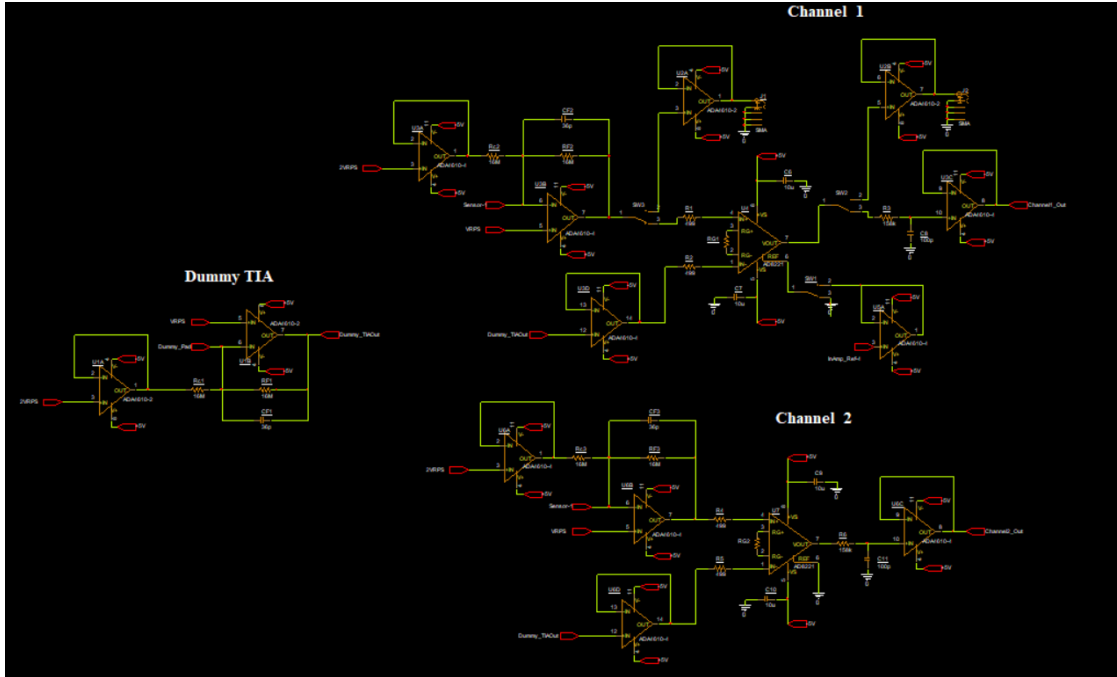


Figure 3.13: Schematics of the first two channels of the second board. The connections for the dummy sensor are also reported. The board consists of 8 channels and, apart for the first having additional testing points, all the additional channels present the same structure as the second one.

Channel	Integrated Noise (μV_{RMS})	RTI Noise (pA_{RMS}).
1	47.2	7.3
2	46.8	7.2
3	50.6	7.8
4	49.2	7.6
5	49.6	7.6
6	48.2	7.4
7	48.3	7.4
8	49.8	7.7

Table 3.3: Integrated noise over the interested bandwidth (0 to 5 kHz) in RMS values referred to the output voltage and reported to the input current for board 2.

Chapter 4

Conclusions

More than forty sensors have been fabricated until the graphitization step to investigate the effect of many parameters on their structure. Protocols have been defined for the NG sensor development, until the definition of a baseline method providing repeatable results and good structure quality of the samples for graphitization aided by iron catalyst. The executed proof-of-concepts experiments reveal some intuitive results, like the graphitization time or the iron chloride concentration employed in the deposited solution, while others reveal some unexpected results as the effect of the flow or the spacer thickness. More analysis should be performed for such tests in order to determine if some other unexpected parameters have been neglected. The reported FSCV measurements reveal a good operation of the NG sensors, being easily able to determine the detection of dopamine concentrations of 500 nM, and presenting stable oxidation and reduction peak positions. From the SEM images is possible to see that some contaminants are present on the island surface, especially after the conditioning phase. In the future, this contaminants should be analyzed in order to understand their origin and try to further prevent their presence. The AFM measurements reveal an increase of the surface roughness and a lowering of the island thickness after the conditioning phase, as an effect of the electrochemical etching of the amorphous carbon. To lower the roughness of the sensors to achieve a better quality, new protocols should be found to increase the crystallinity of the samples to decrease the final roughness and the etching time. The structure implemented for the realization of the interface circuit has been defined after the comparison of different stages and their relative noise measurements. As reported both structures proposed, IN-AMP and PGA channels, and tested show low noise respecting the required performances reported in Table 2.1. From board 1 to board 2 is possible to see an improvement on the noise measurements for the IN-AMP channel, implying an ameliorated design of the second PCB. The second board has been used for the FSCV tests of chapter 2, demonstrating its capabilities for dopamine detection. The next step should be to produce another PCB for the

dedicated digital domain of the interface circuit instead of using an external data acquisition system.

Bibliography

- [1] Wolfgang Mehr, Jarek Dabrowski, J. Christoph Scheytt, Gunther Lippert, Ya-Hong Xie, Max C. Lemme, Mikael Ostling, and Grzegorz Lupina. «Vertical graphene base transistor». In: *IEEE Electron Device Letters* 33.5 (2012), pp. 691–693. DOI: 10.1109/led.2012.2189193 (cit. on p. 1).
- [2] Jinlei Miao and Tingting Fan. «Flexible and stretchable transparent conductive graphene-based electrodes for emerging wearable electronics». In: *Carbon* 202 (2023), pp. 495–527. DOI: 10.1016/j.carbon.2022.11.018 (cit. on p. 1).
- [3] Thomas Mueller, Fengnian Xia, and Phaedon Avouris. «Graphene photodetectors for high-speed optical communications». In: *Nature Photonics* 4.5 (2010), pp. 297–301. DOI: 10.1038/nphoton.2010.40 (cit. on p. 1).
- [4] Liang Zhao, Baichuan Ding, Xian-Ying Qin, Zhijie Wang, Wei Lv, Yan-Bing He, Quan-Hong Yang, and Feiyu Kang. «Revisiting the roles of natural graphite in ongoing lithium-Ion Batteries». In: *Advanced Materials* 34.18 (2022), p. 2106704. DOI: 10.1002/adma.202106704 (cit. on p. 1).
- [5] Zhenyu Zhang, Dorin Simionesie, and Carl Schaschke. «Graphite and hybrid nanomaterials as lubricant additives». In: *Lubricants* 2.2 (2014), pp. 44–65. DOI: 10.3390/lubricants2020044 (cit. on p. 1).
- [6] W.E. Windes, T.D. Burchell, and M. Davenport. «The Advanced Reactor Technologies (ART) graphite R&D program». In: *Nuclear Engineering and Design* 362 (2020), p. 110586. DOI: 10.1016/j.nucengdes.2020.110586 (cit. on p. 1).
- [7] Claudia C. Villarreal, Tung Pham, Pankaj Ramnani, and Ashok Mulchandani. «Carbon allotropes as sensors for environmental monitoring». In: *Current Opinion in Electrochemistry* 3.1 (2017), pp. 106–113. DOI: 10.1016/j.coelec.2017.07.004 (cit. on p. 1).

- [8] Chengguo Hu and Shengshui Hu. «Carbon nanotube-based Electrochemical Sensors: Principles and applications in biomedical systems». In: *Journal of Sensors* 2009 (2009), pp. 1–40. DOI: 10.1155/2009/187615 (cit. on p. 1).
- [9] Edoardo Cuniberto et al. «Nano-engineering the material structure of preferentially oriented nano-graphitic carbon for making high-performance electrochemical micro-sensors». In: *Scientific Reports* 10.1 (2020). DOI: 10.1038/s41598-020-66408-9 (cit. on pp. 1, 2, 6, 7, 12, 13).
- [10] Kae-Dyi You, Edoardo Cuniberto, Shao-Cheng Hsu, Bohan Wu, Zhujun Huang, Xiaochang Pei, and Davood Shahrjerdi. «An Electrochemical Biochip for Measuring Low Concentrations of Analytes With Adjustable Temporal Resolutions». In: *IEEE Transactions on Biomedical Circuits and Systems* 14.4 (2020), pp. 903–917. DOI: 10.1109/TBCAS.2020.3009303 (cit. on pp. 2, 6, 8, 10, 20, 36, 39).
- [11] Rafael Franco, Irene Reyes-Resina, and Gemma Navarro. «Dopamine in health and disease: Much more than a neurotransmitter». In: *Biomedicines* 9.2 (2021), p. 109. DOI: 10.3390/biomedicines9020109 (cit. on p. 5).
- [12] Xixia Liu and Juewen Liu. «Biosensors and sensors for dopamine detection». In: *View* 2.1 (2020), p. 20200102. DOI: 10.1002/viw.20200102 (cit. on pp. 5, 6).
- [13] Anthony A. Grace. «The tonic/phasic model of dopamine system regulation: Its relevance for understanding how stimulant abuse can alter basal ganglia function». In: *Drug and Alcohol Dependence* 37.2 (1995), pp. 111–129. DOI: 10.1016/0376-8716(94)01066-t (cit. on p. 6).
- [14] Julio A. Rodríguez-Manzo, Cuong Pham-Huu, and Florian Banhart. «Graphene growth by a metal-catalyzed solid-state transformation of Amorphous Carbon». In: *ACS Nano* 5.2 (2011), pp. 1529–1534. DOI: 10.1021/nn103456z (cit. on p. 6).
- [15] I.C. Lewis. «6. chemistry of carbonization». In: *Carbon* 20.2 (1982), p. 125. DOI: 10.1016/0008-6223(82)90425-0 (cit. on p. 7).
- [16] A. Oberlin. «Carbonization and graphitization». In: *Carbon* 22.6 (1984), pp. 521–541. DOI: 10.1016/0008-6223(84)90086-1 (cit. on p. 7).
- [17] Noémie Elgrishi, Kelley J. Rountree, Brian D. McCarthy, Eric S. Rountree, Thomas T. Eisenhart, and Jillian L. Dempsey. «A practical beginner’s guide to cyclic voltammetry». In: *Journal of Chemical Education* 95.2 (2017), pp. 197–206. DOI: 10.1021/acs.jchemed.7b00361 (cit. on p. 9).

-
- [18] B. Jill Venton and Qun Cao. «Fundamentals of fast-scan cyclic voltammetry for dopamine detection». In: *The Analyst* 145.4 (2020), pp. 1158–1168. DOI: 10.1039/c9an01586h (cit. on p. 10).
- [19] Chao Chen, Kang Sun, Ao Wang, Siqun Wang, and Jianchun Jiang. «Catalytic graphitization of cellulose using nickel as catalyst». In: *BioResources* 13.2 (2018). DOI: 10.15376/biores.13.2.3165-3176 (cit. on pp. 11, 12).
- [20] Joe Hodkiewicz. 2010. URL: <https://assets.thermofisher.com/TFS-Assets/MSD/Application-Notes/characterizing-graphene-raman-spectroscopy-en-an51946.pdf> (cit. on p. 11).
- [21] Yonggang Zuo et al. «Robust growth of two-dimensional metal dichalcogenides and their alloys by active chalcogen monomer supply». In: *Nature Communications* 13.1 (2022). DOI: 10.1038/s41467-022-28628-7 (cit. on p. 14).
- [22] URL: <https://it.mathworks.com/help/signal/ref/sinad.html> (cit. on p. 27).
- [23] Roy M. Howard. *Principles of Random Signal Analysis and low noise design: The Power Spectral Density and its applications*. Wiley, 2004 (cit. on p. 28).
- [24] Kraig Mitzner, Bob Doe, Alexander Akulin, Anton Suponin, and Dirk Müller. *Complete PCB Design Using OrCAD Capture and PCB Editor*. Newnes, 2019 (cit. on pp. 30, 31).
- [25] Walt Kester. *MT-003:understand Sinad, ENOB, Snr, THD, tHd + N, and SFDR so you don't ...* 2009. URL: <https://www.analog.com/media/en/training-seminars/tutorials/MT-003.pdf> (cit. on p. 33).
- [26] Mahdi Rajabzadeh, Denis Djekic, Matthias Haeberle, Joachim Becker, Jens Anders, and Maurits Ortmanns. «Comparison study of integrated potentiostats: Resistive-TIA, capacitive-TIA, CT $\Sigma\Delta$ modulator». In: *2018 IEEE International Symposium on Circuits and Systems (ISCAS)* (2018). DOI: 10.1109/iscas.2018.8351029 (cit. on pp. 35, 36).
- [27] Download PDF. *Stabilize your transimpedance amplifier*. 2013. URL: <https://www.analog.com/en/technical-articles/stabilize-transimpedance-amplifier-circuit-design.html> (cit. on p. 36).
- [28] Chunfeng Bai, Jianhui Wu, and Xiaoying Deng. «A review of CMOS variable gain amplifiers and programmable gain amplifiers». In: *IETE Technical Review* 36.5 (2018), pp. 484–500. DOI: 10.1080/02564602.2018.1507766 (cit. on pp. 36, 37).
- [29] Charles Kitchin and Lew Counts. *Education library*. 2006. URL: <https://www.analog.com/en/education/education-library/dh-designers-guide-to-instrumentation-amps.html> (cit. on p. 38).